Annu. Rev. Astronomy Astrophysics 2014 54

Micro-Arcsecond Radio Astrometry

M.J. Reid
Harvard-Smithsonian Center for Astrophysics, 60 Garden Street, Cambridge, MA 02138, U.S.A.

M. Honma
Mizusawa VLBI Observatory, National Astronomical Observatory of Japan & Department of Astronomical Science, The Graduate University for Advanced Study, Mitaka 181-8588, Japan

Key Words

Distance, Parallax, Proper Motion, VLBI, Galactic Structure, Star Formation, Evolved Stars, Pulsars, Hubble Constant

Abstract

Astrometry provides the foundation for astrophysics. Accurate positions are required for the association of sources detected at different times or wavelengths, and distances are essential to estimate the size, luminosity, mass, and ages of most objects. Very Long Baseline Interferometry at radio wavelengths, with diffraction-limited imaging at sub-milliarcsec resolution, has long held the promise of micro-arcsecond astrometry. However, only in the past decade has this been routinely achieved. Currently, parallaxes for sources across the Milky Way are being measured with ~ 10 μas accuracy and proper motions of galaxies are being determined with accuracies of ~ 1 μas y^{-1}. The astrophysical applications of these measurements cover many fields, including star formation, evolved stars, stellar and super-massive black holes, Galactic structure, the history and fate of the Local Group, the Hubble constant, and tests of general relativity. This review summarizes the methods used and the astrophysical applications of micro-arcsecond radio astrometry.

1 Introduction

1.1 History

For centuries astrometry was the primary focus of astronomy. Before the 17th century, astronomers charted the locations of naked-eye stars with an accuracy of a fraction of an arcminute. With this level of accuracy, all but a handful of the highest proper motion stars remain "fixed" for an astronomer's lifetime, and it was not until Galileo's introduction of the telescope in astronomy that arcsecond precision became a possibility.

For millennia two great questions remained unanswered: was the Earth at the center of the Universe and how large was the Universe? Both questions could be answered through astrometry by measuring the parallax of stars. If the Earth revolved around the Sun, stars would exhibit yearly shifts in apparent position (annual parallax) and, if measured, these would indicate their distances (at that time equivalent to the "size of the Universe"). This scientific opportunity led most scientists of the period to attempt astrometric measurements to detect parallax (Hirshfeld 2001).

Early attempts to measure parallax by Robert Hooke, and later James Bradley, compared the tilt of a near-vertical telescope to that of a plumb-line as the star γ Draconis transited directly overhead in London. Bradley, after discovering and accounting for aberration of light (a yearly ± 20 arcsec effect caused by the Earth's orbital motion), was only able to place an upper limit of 0.5 arcsec on the annual parallax of the star. It was not until 1838 that Friedrich Wilhelm Bessel presented the first convincing measurement of stellar parallax: 0.314 arcsec for the star 61 Cygni (chosen as a candidate by its large proper motion of ≈ 5 arcsec yr^{-1}).

Bessel and others followed a suggestion attributed to Galileo to measure *relative* parallax, the differential position shift of a nearby target star relative to a distant background star, rather than *absolute* position shifts. This approach still forms the basis of the highest accuracy measurements made today. Currently astrometric accuracy using Very Long Baseline Interferometry (VLBI) at centimeter wavelengths is approaching the ~ 1 μas level. This review documents the state of the art in radio astrometry, focusing both on the techniques and the scientific results.

1.2 Radio Astrometry

Karl Jansky made the first astronomical observations at radio wavelengths in the 1920s. While searching for the source of interference in trans-atlantic telephone calls (mostly from lightning in the tropics), he noted strong emission localized within a few degrees in the constellation of Sagittarius. The peak of the signal drifted in time at a sidereal rate, indicating an origin outside the Solar System, and was ultimately traced to energetic (synchrotron emitting) electrons throughout the Milky Way, but concentrated toward the center.

The development of radar during WWII, gave a boost to radio astronomy in the 1940s and 1950s. Astrometric precision with a single radio telescope was generally limited to some fraction of the diffraction limit, $\theta_d \approx \lambda/D$, where λ is the observing wavelength and D is the antenna diameter. Even though radio antennas were an order of magnitude larger than optical telescopes, the roughly four orders of magnitude longer wavelength seemed to doom radio astrometry. However, that changed with the development of radio interferometry. In the 1960s, interferometers with baselines of ~ 1 km localized the positions of quasi-stellar objects (QSOs), leading to the discovery of highly redshifted optical emission. Over the years, with increasing baseline length, positional accuracy with (connected-element) interferometers improved from ~ 1 to ~ 0.03 arcseconds (Wade & Johnston 1977).

In the late 1960s, radio interferometry was greatly extended by removing the need for a direct connection (either with cables or microwave links) between antennas. Signals were accurately time tagged using independent atomic clocks and recorded on magnetic tape, allowing separations of interferometer elements across the Earth. This technique, called Very Long Baseline Interferometry (VLBI), lead to many discoveries, including super-luminal motion in jets from active galactic nuclei (AGN) and upper limits of ~ 1 pc on the size of the emitting regions. Both results provided strong evidence for super-massive black holes as the engines for AGN (Reid 2009). Early VLBI observations with intrinsic angular resolution better than 1 mas offered absolute position accuracy of ~ 0.3 mas using group-delay observables (Clark et al. 1976; Ma et al. 1986) and relative astrometric accuracy between fortuitously close pairings of QSOs of ~ 10 μas using phase-delay information (Marcaide et al. 1985).

Starting in the 2000s, calibration techniques improved to the point where relative positional accuracy of ~ 10 μas could be routinely achieved for most bright targets, relative to a detectable QSO usually within a couple of degrees on the sky. This changed the game dramatically. Such astrometric accuracy is unsurpassed in astronomy and is comparable to, or better than, the target accuracy of the next European astrometric space mission: Gaia (Bourda et al. 2011). Since radio waves are not absorbed significantly by interstellar dust, the entire Milky Way is available for observation. Also, since QSOs are used as the position reference, *absolute* parallax and proper motions are directly measurable. Such measurements for over 100 star forming regions have now been made for sources as distant as 11 kpc. Significant results (see §2) include a resolution of the Hipparcos Pleiades distance controversy (Melis et al. 2014), 3-dimensional "imaging" of nearby star forming regions (Loinard et al. 2007), and the most accurate measurements to date of the distance to the Galactic Center, R_0, and the circular rotation speed of the Local Standard of Rest, Θ_0 (Reid et al. 2014).

2 Astrophysical Applications

Since distance is fundamental to astrophysical understanding, it should not be surprising that radio astrometry and parallax measurements are critical for characterizing a wide variety of phenomena and classes of sources. Here we briefly discuss some of the more important astrophysical applications of radio astrometry.

2.1 Galactic Structure

Surprisingly, we know little of the spiral structure of the Milky Way; there is considerable debate over the number of spiral arms, the nature of the central bar, and the values of the fundamental parameters R_0 (distance to Galactic center) and Θ_0 (circular rotation speed of the LSR). Major projects are underway to map the Milky Way with the VLBI Exploration of Radio Astrometry (VERA) array and the Very Long Baseline Array (VLBA) array, though the Bar and Spiral Structure Legacy (BeSSeL) survey. With typical parallax accuracy of ± 20 μas, and best accuracy of ± 5 μas, one can measure distances of 5 and 20 kpc, respectively, with $\pm 10\%$ accuracy. For example, parallax data for the most distant source measured to date, the massive star forming region W 49, are shown in **Figure 1**. Over 100 distances to high-mass star forming regions have been measured using the astronomical "gold standard" technique of trigonometric parallax (see Reid et al. (2009b); Honma et al. (2012); Reid et al. (2014) and references therein).

Attempts to decode the nature of the spiral structure of the Milky Way have long relied on kinematic distance estimates (by comparing the Doppler velocity of a source and that expected from a model of Galactic rotation with distance as a free parameter). One of the first high-precision VLBA parallaxes was for the massive star forming region W3(OH); Xu et al. (2006) found a distance of 1.95 ± 0.04 kpc, confirmed by Hachisuka et al. (2006). This distance was more than a factor of two less than its kinematic distance, demonstrating how unreliable kinematic distances can be. Now, with "gold standard" trigonometric parallaxes,

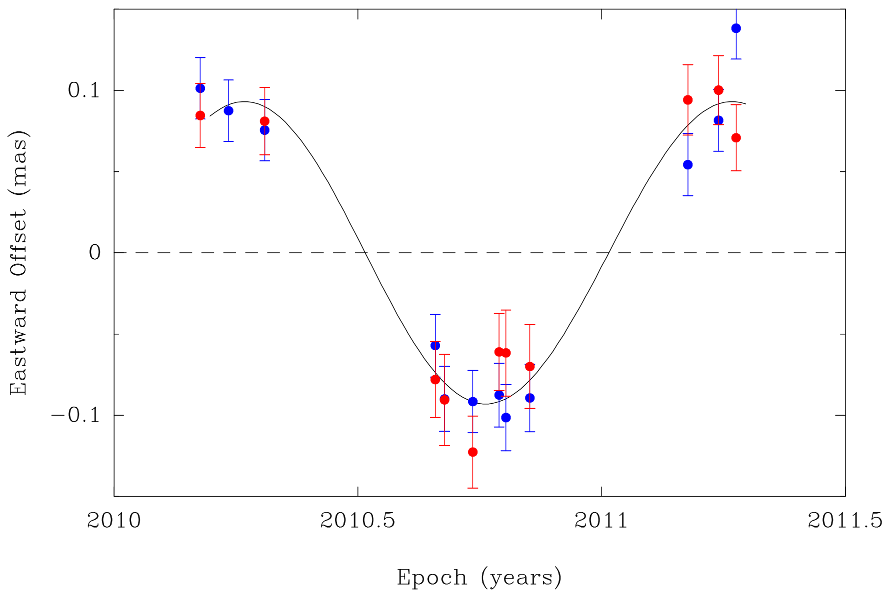

Figure 1:

Parallax data for W 49N measured with the VLBA after Zhang et al. (2013). Plotted are eastward position offsets versus time for H_2O maser spots at an LSR velocity of 8.3 km s^{-1} relative to the background quasar J1905+0952 (shown in red) and a maser spot at an LSR velocity of 4.9 km s^{-1} relative to the background quasar J1922+0841 (shown in blue). The best fit proper motion has been removed, allowing the data to be overlaid and effects of parallax to be more clearly seen. This source has a parallax of 0.090 ± 0.006 mas, corresponding to a distance of 11.1 ± 0.8 kpc.

the major spiral features of the Milky Way are, for the first time, being accurately located and spiral arm pitch angles measured (see **Figure 2**). Recent surprises include that the Local (Orion) arm, thought to be a minor structure, is longer and has far more on-going star formation than previously thought and rivals the Perseus spiral arm in the second and third Galactic quadrants (Xu et al. 2013).

With measured source coordinates, distance, proper motion, and radial velocity, one has full phase-space (3-dimensional position and velocity) information. These data can be modeled to yield an estimate of R_0, Θ_0, and the slope of the Galaxy's rotation curve. The latest modeling indicates that $R_0 = 8.35 \pm 0.16$ kpc and $\Theta_0 = 251 \pm 8$ km s^{-1} (Reid et al. 2014). Also, the rotation curve between 4 and 13 kpc from the Galactic center is very flat (Honma et al. 2007; Reid et al. 2014). Such a large value for Θ_0 (about 15% larger than the IAU recommended value of 220 km s^{-1}), if confirmed by other measurements, would have widespread impact in astrophysics, including increasing the total mass (including dark matter halo) of the Milky Way by about 50%, revising Local Group dynamics by changing the Milky Way's mass and velocities of Group members (when transforming from Heliocentric to Galactocentric coordinate systems), and increasing the expected signal from dark matter annihilation radiation.

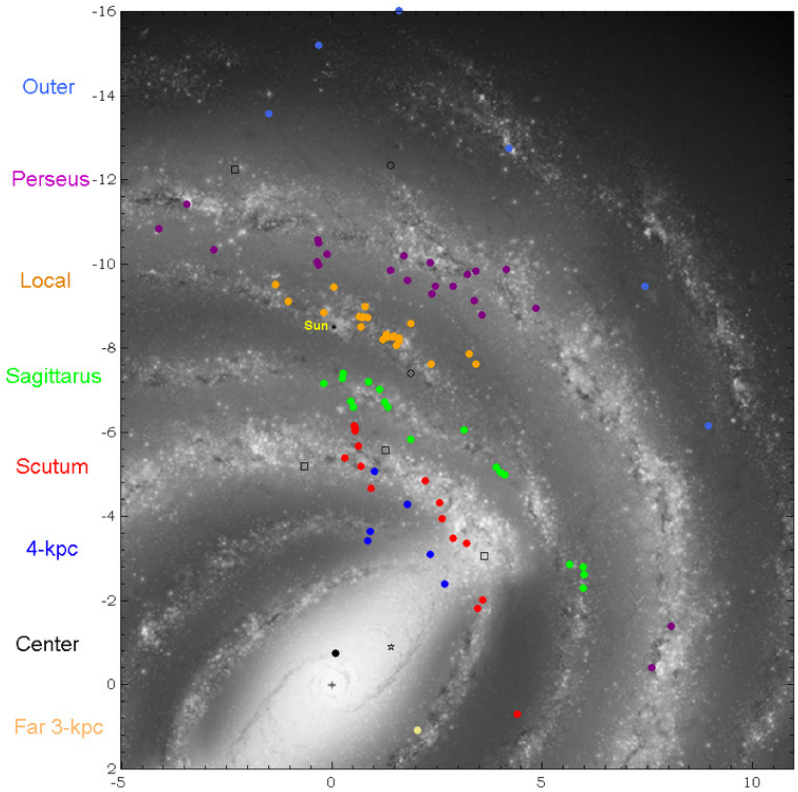

Figure 2:

Plan view of Milky Way. The background is an artist conception, guided by VLBI astrometry and Spitzer Space Telescope photometry (R. Hurt: IPAC). Dots are the locations of newly formed OB-type stars determined from trigonometric parallaxes using associated maser emission. The parallaxes were determined with the VLBA, VERA, and the EVN. Assignment to spiral arms (indicated by dot color) has been made by comparison to large scale emission of carbon monoxide in Galactic longitude–Doppler velocity space, independent of distance. The Galactic center is denoted by the plus (+) sign at (0,0) kpc; the Sun is labeled in yellow at (0,8.4) kpc. On this view, the Milky Way rotates clockwise.

2.2 Star Formation

Gould's Belt, a flattened structure of star forming regions of radius ≈ 1 kpc and centered ≈ 0.1 kpc from the Sun (toward the Galactic anticenter), contains most of the sites of current star formation near the Sun (e.g., the Ophiucus, Lupus, Taurus, Orion, Aquila Rift and Serpens star forming regions). Most of our knowledge about the formation of stars like the Sun comes from in-depth studies of these regions, for example, from the Spitzer c2d survey (Evans et al. 2009), the XMM Newton Extended Survey of Taurus (Güdel et al. 2008) and the Herschel Gould Belt Survey (André et al. 2010). Of course, knowledge of distance is critical for quantitative measures of cloud and young stellar object (YSO) sizes, masses, luminosities and ages. For such deeply embedded sources, which are optically invisible, typically distances had not been estimated to an accuracy of better than ±30%. Since some physical parameters depend on distance squared or cubed, these parameters can be in error by factors of ≈ 2.

Trigonometic parallax measurements with VLBI techniques can be made by observing gyro-synchrotron emission from T Tauri objects, which is usually confined to a region of a few stellar radii, or from H_2O maser emission often associated with Herbig-Haro outflows. Currently, about a dozen YSOs parallaxes have been obtained, with up to 200 planned in this decade.

In the Ophiucus cloud, Loinard et al. (2008), using the VLBA, found that sources S1 and DoAr21 are at a mean distance of 120.0 ± 4.5 pc; Imai et al. (2007) using VERA found a consistent distance of 178^{+18}_{-37} pc, albeit with larger uncertainty, for the H_2O masers toward IRAS 16293−2422. The Taurus molecular cloud has been well studied and parallaxes for five YSOs have been reported from VLBA observations in a series of papers (Loinard et al. 2005, 2007; Torres et al. 2007, 2009, 2012). These locate three YSOs associated with the L 1495 dark cloud at a distance of 131.4 ± 1.4 pc and, interestingly, T Tauri Sb at 146.7 ± 0.6 pc and HP Tau/G3 at 161.9 ± 0.9 pc. Clearly, these observations are tracing the 3-dimensional structure of the cloud, which is extended over about 30 pc along the line of sight, consistent with its extent on the sky of 10° (≈ 25 pc).

VERA observations have yielded parallaxes to YSOs in the Perseus molecular cloud. Observing H_2O masers, Hirota et al. (2008) measured parallax distances of 235 ± 18 pc for the SVS 13 toward NGC 1333 and 232 ± 18 pc for L 1448 C (Hirota et al. 2011). These measurements clarified the distance to the Perseus cloud, which was highly uncertain – estimated at between 220 pc (Cernis 1990) and 350 pc (Herbig & Jones 1983). The Serpens cloud provides another example where previous optical-based distance estimates varied considerably from 250 to 700 pc, with recent convergence toward the low end at $\sim 230 \pm 20$ pc, as summarized by Eiroa, Djupvik & Casali (2008). However, Dzib et al. (2010) used the VLBA to obtain a trigonometric parallax distance for EC 59 of 414.9 ± 4.4 pc and suggested that faulty identification of dusty clouds in the foreground Aquila Rift might account for optical distance estimate.

The Orion Nebula is perhaps the most widely studied region of star formation. Prior to 1981, distance estimates for the Orion Nebula ranged from about 380 to 520 pc as summarized by Genzel et al. (1981). By comparing radial and proper motions (measured with VLBI observations) of H_2O masers toward the Kleinman–Low (KL) Nebula, an active region of star formation within the Orion Nebula, Genzel et al. estimated the distance to be 480 ± 80 pc. Since then, four independent trigonometric parallax measurements have been performed. Sandstrom et al. (2007) observed gyro-synchrotron emission from a YSO over nearly 2 yr and obtained a parallax distance of 389 ± 24 pc using the VLBA. Hirota et al. (2007) using VERA measured H_2O masers and determined a distance of 437 ± 19 pc for the KL region. Recently, two very accurate parallaxes have been published: Menten et al. (2007) used the VLBA and observed continuum emission from three YSOs and determined a distance of 414 ± 7 pc; Kim et al. (2008) using VERA and observing SiO masers estimated a distance of 418 ± 6 pc. The latter two measurements from different groups, using different VLBI arrays, different target sources, and different correlators and software are in excellent agreement. Together they indicate that the KL nebula/Trapezium region of the Orion Nebula is at a distance of 416 ± 5pc, nearly a 1% accurate distance! Since, the Orion Nebula is the subject of large surveys, from x-rays to radio waves, having such a "gold-standard" distance will enable precise estimates of sizes, luminosities, masses, and ages.

A large number (> 100) of parallaxes have been measured with the VLBA and EVN arrays for maser sources in high mass star forming regions (Bartkiewicz et al. 2008; Brunthaler et al. 2009; Hachisuka et al. 2009; Mollenbrock, Claussen & Goss 2009; Sanna et al. 2009; Xu et al. 2009; Zhang et al. 2009; Rygl et al. 2010; Sato et al. 2010a; Moscadelli et al. 2011; Xu et al. 2011; Sanna et al. 2012; Immer et al. 2013) and by the VERA array (Sato et al. 2008, 2010b; Oh et al. 2010; Ando et al. 2011; Honma et al. 2011; Kurayama et al. 2011; Matsumoto et al. 2011; Motogi et al. 2011; Nagayama et al. 2011a,b; Niinuma et al. 2011; Shiozaki et al. 2011; Sakai et al. 2012). As the focus of these observations has been to better understand Galactic structure, we discuss these in §2.1.

2.3 Asymptotic Giant Branch Stars

Asymptotic Giant Branch (AGB) stars are in late stages of stellar evolution and have large convective envelopes and high mass-loss rates. They often exhibit maser emission from circumstellar OH, H_2O and SiO molecules, providing good targets for radio astrometry with VLBI. Accurate distances to AGB stars are necessary to constrain their physical parameters, such as size and luminosity, and these are crucial to test theories of late stages of stellar evolution. And, of course, distances are needed to calibrate the period-luminosity (P-L) relation of Mira variables, which can be used as standard candles, e.g., Whitelock, Feast & Van Leeuwen (2008). Giant stars are not good astrometric targets at optical wavelengths and the best optical parallaxes have accuracies poorer than a few mas. However, parallaxes based on radio observations of circumstellar masers has demonstrated more than a factor of ten better parallax accuracy, allowing much better calibration of the Mira P-L relation.

Early astrometric observations with the VLBA for red-giant OH masers demonstrated the potential for parallax measurements, achieving between 0.3 and 2 mas uncertainties ((Langevelde et al., 2000; Vlemmings et al., 2003)). For example, parallax distances for S CrB (418^{+21}_{-18} pc) and U Her (266^{+32}_{-28} pc) by Vlemmings & Langevelde (2007) are considerably more accurate than those measured by the Hipparcos satellite. Astrometry of OH masers at the relatively low observing frequency of 1.6 GHz are limited by uncompensated ionospheric effects, but these effects can be minimized by observations near solar minimum and using in-beam calibrators very close to the targets.

The first VLBI parallax of an AGB star using H_2O masers at 22 GHz revealed a distance for UX Cyg, a long period Mira variable, of $1.85^{+0.25}_{-0.19}$ kpc (Kurayama, Sasao & Kobayashi 2005). Since then the VERA array has been used to obtain parallaxes for many Mira and semi-regular variables, including S Crt (Nakagawa et al. 2008), SY Scl (Nyu et al., 2011), and RX Boo (Kamezaki et al. 2012). Of particular interest are the astrometric measurements for the symbiotic system R Aqr (Kamohara et al. 2010) and the parallax distance of 218^{+12}_{-11} pc (Min et al. 2013). Future observations may enable one to trace binary's orbital motion.

Red supergiants are rare objects, typically at kpc distances. At these distances, and owing to their very large sizes and irregular photospheres, they are beyond the reach of optical parallax measurements. Choi et al. (2008) observed H_2O masers toward VY CMa, one of the best-studied red supergiants, and found a parallax distance of $1.14^{+0.11}_{-0.09}$ kpc with VERA. This distance was later confirmed by Zhang et al. (2012b), who used the VLBA and found a distance of $1.20^{+0.13}_{-0.10}$ kpc. Generally, the distance had been assumed to be 1.5 kpc, requiring an extraordinary luminosity of 5×10^5 $L_\odot$; the parallax distances reduce the luminosity estimate by 40% to a more reasonable value. VLBI parallaxes accurate to ±10% have been obtained for several other red supergiants, including S Per (Asaki et al. 2010), NML Cyg (Zhang et al. 2012b), and IRAS 22480+6002 (Imai et al. 2012).

Proto-Planetary Nebulae are in the final stage of evolution of intermediate-mass stars, linking the AGB and planetary nebula phases. These sources are known to exhibit bipolar outflows with a velocities exceeding ∼100 km s^{-1}; they can have strong H_2O masers and are often called "water-fountains." Parallaxes have been measured for IRAS 19134+2131 (Imai, Sahai & Morris 2007, IRAS 19312+1950 (Imai et al. 2011), IRAS 18286-0959 (Imai et al. 2013), and K 3-35 (Tafoya et al. 2011).

2.4 X-ray Binaries

The first trigonometric parallax for a black hole candidate was for the X-ray binary V404 Cyg (Miller-Jones et al. 2009), indicating a distance of 2.39 ± 0.14 kpc. This value was significantly lower than previously estimated and indicated that its 1989 outburst was not super-Eddington. Its peculiar velocity, derived from the radio proper motion, is only about 40 km s^{-1}, suggesting that it did not receive a large natal "kick" from an asymmetric supernova explosion. This differs from many pulsars, which often have order of magnitude larger peculiar motions (see §2.5).

The long-standing uncertainty over the distance to Cyg X-1 (see, e.g.,, Caballero-Nieves et al. (2009)) limited understanding of this famous binary, including whether or not the unseen companion was a black hole. Recently a trigonometric parallax measurement with the VLBA yielded a distance of 1.86 ± 0.12 kpc (Reid et al. 2011). Knowing the distance to the binary removed the mass–distance degeneracy that limited the modeling of optical/IR data (light and velocity curves) and revealed that the unseen companion in Cyg X-1 has a mass of 14.8 ± 1.0 $M_{\odot}$ (Orosz et al. 2011). This mass confidently exceeds the limit for a neutron star and firmly established it as a black hole. Once the masses of the two stars were accurately determined, X-ray data could be well modeled. This revealed that black hole spin is near maximal and, since the binary is too young for accretion to have appreciably spun up the black hole, most of the spin angular momentum is probably natal (Gou et al. 2011). Finally, the 3-dimensional space-motion of the binary, from the radio astrometry and optical Doppler shifts, confirms Cyg X-1 as a member of the Cyg OB3 association, and the lack of evidence for a supernova explosion in this region suggests that the black hole may have formed via prompt collapse without an explosion (Mirabel & Rodigues 2003).

Recently, using the EVN and the VLBA, Miller-Jones et al. (2013) obtained a parallax distance of 114 ± 2 pc for SS Cyg, a binary composed of a white and red dwarf. This distance is significantly less than an optical parallax measured with the Hubble Space Telescope of 159 ± 12 pc (Harrison et al. 1999). The larger optical distance required the source to be significantly more luminous and proved difficult to reconcile with accretion disk theory. However, the smaller distance from radio astrometry seems to resolve this problem.

2.5 Pulsars

Pulsar radio emissions are extremely compact and relatively bright, which make them suitable for VLBI observations, and radio astrometry of pulsars dates back to the 1980's. The first interferometric parallax measurements were by Gwinn et al. (1986), who reported parallaxes for two pulsars using a VLBI array which included the Arecibo 305-m telescope. Later Bailes et al. (1990a) measured a parallax for PSR 1451−68 of 2.2 ± 0.3 mas, using the Parkes–Tidbinbilla Interferometer in Australia, and determined a line-of-sight average interstellar electron density of 0.019 ± 0.003 cm^{-3} by combining the distance and dispersion measures, suggesting that the interstellar medium in the Solar neighborhood is typical of that over larger scales in the Galaxy. Pulsar proper motions for 6 pulsars conducted with the Parkes–Tidbinbilla Interferometer revealed that motions away from the Galactic plane were between 70 and 600 km s^{-1} (Bailes et al. 1990b). These early studies provided distances and confirmed the expectation that pulsars are high-velocity objects, most-likely due to "kicks" associated with their parent supernova explosions.

Most recent pulsar astrometry uses "in-beam" calibrators to greatly improve positional accuracy. Other improvements include gating the pulsar signal during correlation to improve signal-to-noise ratios and performing ionospheric corrections based on multi-frequency phase fitting. With these improvements and using the VLBA a parallax with better than $\pm 10\%$ accuracy was obtained for PSR B0950+08 at a distance of 280 pc (Brisken et al. 2000), and nine other pulsar parallaxes with distances between 160 and 1400 pc have been reported (Brisken et al. 2002).

By observing at higher frequencies (5 GHz instead of 1.6 GHz), in order to reduce the effects of the ionosphere, higher accuracy pulsar parallaxes have been obtained, for example, for PSR B0355+54 (0.91 ± 0.16 mas) and PSR B1929+10 (2.77 ± 0.07 mas) (Chatterjee et al. 2004). More recently, Chatterjee et al. (2009) obtained results for 14 pulsars with the VLBA, including a parallax for the most distance pulsar yet measured: PSR B1514+09 with a parallax of 0.13 ± 0.02 mas, corresponding to a distance of $7.2^{+1.3}_{-1.2}$ kpc. With this sample, it is clear that most pulsars are moving away from the Galactic plane with speeds of hundreds of km s^{-1}.

Astrometry also provides a unique opportunity to constrain pulsar birth places through velocity and distance measurements. For instance, Campbell et al. (1996) used a global VLBI array to measure the parallax and proper motion for PSR B2021+51, which ruled out the supernova remnant HB 21 as the origin of the pulsar, as it implied an improbable low age of only 700 years. Similar studies have been performed by others (Dodson et al. 2003; Ng et al. 2007; Chatterjee et al. 2009; Bietenholz et al. 2013).

Astrometric observations also provide information on the physical properties of pulsars. For example, Brisken et al. (2003) combined a VLBA parallax for PSR B0656+14 with a thermal X-ray emission model to constrain the stellar radius between 13 and 20 km. Deller et al. (2012b) measured a parallax for the transitional millisecond pulsar J1023+0038 with the VLBA. Their distance of 1368^{+42}_{-39} pc was twice that predicted by the standard interstellar plasma model. When combined with timing and optical observations of this binary system, the new distance indicated a mass of $M \sim 1.71 \pm 0.1\ M_{\odot}$, suggesting that it is a recycled pulsar. Deller et al. (2009b) conducted astrometric observations of seven pulsars in the southern hemisphere using Australian Long Baseline Array (LBA). Their new distance to PSR J0630−2834 required the efficiency of conversion of spin-down energy to X-rays to be less than 1%, an order of magnitude lower than previous estimates using a less accurate distance.

Magnetars, pulsars with extremely strong magnetic field, are also interesting astrometric targets. Helfand et al. (2007) observed XTE J1810−197 with the VLBA and obtained a proper motion of 212 km s^{-1}, suggesting that this magnetar has a lower space motion than theoretical predicted (Duncan & Thompson 1992). Recently, Deller et al. (2012a) found a similarly low space motion for the magnetar J1550−5418.

Finally, pulsar astrometry can be critical for testing the constancy of physical parameters. Using the VLBA, Deller et al. (2008) observed J0437−4715, a milli-second binary pulsar with a white dwarf companion. They obtained a very precise parallax distance of 156.3 ± 1.3 pc. Comparing this to a kinematic distance from pulsar timing gives strong limits on unmodeled accelerations, which provide a limit on the constancy of the Gravitational constant of $\dot{G}/G = (-5 \pm 26) \times 10^{-13}$ yr^{-1}. This constraint is consistent with those obtained from lunar laser ranging as well as gravitational wave backgrounds.

2.6 Radio Stars

The Algol system is an eclipsing binary (with a period of 2.9 days, consisting of B8 V primary and K0 IV secondary) and a distant companion with an orbital period of 1.86 yr. VLBI astrometry by Lestrade et al. (1993) revealed that the radio emission originates from the K0 subgiant and traced the orbital motion of eclipsing binary, indicating that the orbit of the binary is nearly orthogonal to that of the tertiary companion. Observations of another hierarchical triple (Algol-like) system, UX Ari, by Peterson et al. (2011) detected the acceleration of the tight binary caused by the tertiary star. This acceleration measurement dynamically constrains the mass of the tertiary to be $\approx 0.75\ M_\odot$, a value consistent with a spectroscopic identification of a K1 main-sequence star.

Astrometric observations of radio stars allow one to accurately tie the fundamental radio and the optical reference frames. A comparison between the radio and preliminary Hipparcos frames by Lestrade et al. (1995) revealed systematic discrepancies that could be removed by a global rotation (and its time derivative). Further VLBI observations by Lestrade et al. (1999) achieved parallax accuracies of ≈ 0.25 mas for nine sources, whose distances ranged from 20 to 150 pc.

Dzib et al. (2013) monitored radio emission from colliding winds in Cyg OB2#5 and obtained a marginal parallax of 0.61 ± 0.22 mas, consistent with other distance measurements of Cyg X regions (Rygl et al. 2012; Zhang et al. 2012b). These observations also revealed a high radio-brightness temperature ($\gtrsim 10^7$ K), providing information for modeling the stellar winds.

2.7 Star Clusters

The Hyades and Pleiades clusters play a pivotal role in quantitative astrophysics, serving as pillars of the astronomical distance ladder. Recently, the Hipparcos space mission, which measured $\approx 100,000$ stellar parallaxes with typical accuracies of ± 1 mas, presented a (revised) parallax distance of 120.2 ± 1.9 pc for the Pleiades (van Leeuwen 2009). This result has been quite controversial, since a variety of other techniques, including main-sequence fitting, generally give distances between 131 and 135 pc. Using the HST fine guidance sensor, Soderblom et al. (2005) measured *relative* trigonometric parallaxes for three Pleiads, which, after correction to absolute parallaxes, average to a distance of 134.6 ± 3.1 pc.

In an attempt to provide a totally independent and straight-forward distance to the Pleiades, Melis et al. (2014) have used the VLBA with the Green Bank and Arecibo telescopes to measure *absolute* parallaxes to several Pleiads that display compact radio emission. Preliminary results suggest a cluster parallax near 138 pc, with an uncertainty of less than ± 2 pc (including measurement error and cluster depth effects). This result seems to rule out the Hipparcos value, and it may even be in some tension with the ensemble of astrophysical-based distance indicators. Since the source of error for the Hipparcos parallax for the Pleiades has not been convincingly established, there could be concern for the Gaia mission, which is targeting a parallax accuracy of $\pm 20\ \mu$as, since Gaia might inherit some unknown systematics from Hipparcos. Intercomparison of high accuracy VLBA parallaxes with those from Gaia will provide a critical cross checking.

2.8 Sgr A*

Sgr A*, the candidate super-massive black hole (SMBH) at the center of the Galaxy, is a strong radio source. It is precluded from optical view by > 20 mag of visual extinction but can sometimes be detected when flaring at 2.2 μm wavelength (through $\lesssim 3$ mag of extinction at this wavelength). Astrometric observations in the infrared of stars orbiting an unseen mass have provided compelling evidence of a huge mass concentration, almost surely a black hole (Ghez et al. 2008; Gillessen et al. 2009). These observations require a grid of sources with accurate positions relative to Sgr A* to calibrate the infrared plate scale, rotation, and low-order distortion terms. The calibration sources have been provided by VLA and VLBA astrometric observations relative to the radio bright Sgr A* of SiO and H_2O masers in the circumstellar envelopes of red giant and supergiant stars within the central pc (Reid et al. 2003). This allowed location of the position of Sgr A* on infrared images, which matched that of the gravitational focal position of the stellar orbits to ≈ 1 mas accuracy, as well as confirming Sgr A*'s extremely low luminosity (Menten et al. 1997).

Astrometric observations of Sgr A* at 7 mm wavelength, relative to background quasars with the VLBA, yielded the angular motion of the Sun about the Galactic center and placed extremely stringent limits on the mass density of the SMBH candidate. While stars orbiting Sgr A* have been observed to move with speeds exceeding 5000 km s^{-1} (Schödel et al. 2002), the velocity component perpendicular to the Galactic plane of Sgr A* is less than ≈ 1 km s^{-1}, requiring that most of the $4 \times 10^6\ M_\odot$ required by the stellar orbits is tied to the radiative source Sgr A* (Reid & Brunthaler 2004). Since the millimeter wavelength emission from Sgr A* is confined to a ~ 1 Schwarzschild radii region (Doeleman et al. 2008), the implied mass density is approaching that theoretically expected for a black hole (Reid 2009).

2.9 Megamasers and the Hubble Constant

The Hubble constant, H_0, is a critical cosmological parameter, not only for the extragalactic distance scale, but also for determining the flatness of the Universe and the nature of dark energy. Some active galactic nuclei (AGN) with thin, edge-on accretion disks surrounding their central super-massive black hole (SMBH) exhibit H_2O "megamaser" emission, with bright maser spots coming from clouds in Keplerian orbit about the SMBH. Astrometric observations can be used to map the positions and velocities of these clouds. Coupled with time monitoring of the maser spectra, which allows direct measurement of cloud accelerations (by tracking the velocity drift over time of maser features), one can obtain a geometric (angular-diameter) distance estimate for the galaxy.

Observations of the archetypal megamaser galaxy, NGC 4258, demonstrated the power of radio astrometric observations for better understanding of AGN accretion disks (Herrnstein et al. 2005) and yielded an accurate distance of 7.2 ± 0.5 Mpc to the galaxy (Herrnstein et al. 1999). Since NGC 4258 is nearby and its (unknown) peculiar motion is likely to be a large fraction of its cosmological recessional velocity (≈ 500 km s^{-1}), one cannot directly measure H_0 by dividing velocity by distance. However, since Cepheid variables have been observed in NGC 4258, one can use the radio distance to recalibrate the zero-point of the Cepheid period-luminosity relation (Macri et al. 2006) and then revise estimates of H_0 (Riess, Fliri & Valls-Gabaud 2012; Riess et al. 2012). Recently, Humphreys et al. (2013) analyzed a decade of observations of NGC 4258 and, via more detailed modeling of disk kinematics, obtained an extremely accurate distance of 7.60 ± 0.23 Mpc, which constrains

$H_0 = 72.0 \pm 3.0$ km s^{-1} Mpc^{-1}.

By observing H_2O masers in galaxies like NGC 4258, but more distant and well into the "Hubble flow," the Megamaser Cosmology Project (MCP) is obtaining direct estimates of H_0. For galaxies in the Hubble flow, unknown galaxy peculiar motions are a small source of systematic uncertainty ($\lesssim 5\%$). Results for the megamaser galaxy UGC 3789 (Reid et al. 2009c; Braatz et al. 2010) have yielded $H_0 = 68.9 \pm 7.1$ km s^{-1} Mpc^{-1} (Reid et al. 2013) and for NGC 6264 $H_0 = 68 \pm 9$ km s^{-1} Mpc^{-1} (Kuo et al. 2013). Based on these results, and preliminary results for Mrk 1419, Braatz et al. (2013) find a combined result of $H_0 = 68.0 \pm 4.8$ km s^{-1} Mpc^{-1}. The goal of the MCP is measurement of ≈ 10 megamaser galaxies, each with an accuracy near $\pm 10\%$, which should yield a combined estimate of H_0 with $\pm 3\%$ accuracy. While, formally, a $\pm 3\%$ uncertainty may be slightly larger than claimed by other techniques, the megamaser method is direct (not dependent on standard candles) and totally independent.

2.10 Extragalactic Proper Motions

In the concordance ΛCDM cosmological model, galaxies grow hierarchically by accreting smaller galaxies. Nearby examples of galaxy interactions are found in the environments of the Milky Way and the Andromeda Galaxy, the dominant galaxies in the Local Group. In the past, only *radial* velocities for Local Group galaxies were known and statistical approaches had to be used to model the system. While the radial velocity of Andromeda indicates that it is approaching the Milky Way, without knowledge of its proper motion one cannot know, for example, if the two galaxies are on a collision course or if they are in a relatively stable orbit.

Astrometric VLBI observations have yielded both the internal angular rotation and the absolute proper motion of M 33, a satellite of Andromeda (Brunthaler et al. 2005). The angular rotation of M33 was the focus of the van Maanen–Hubble debate in the 1920's (van Maanen 1923; Hubble 1926), with van Maanen claiming an angular rotation of 20 ± 1 mas y^{-1}. Such a large angular rotation required it to be nearby and part of the Milky Way, in order to avoid implausibly large rotation speeds. Indeed, Shapley forwarded this as evidence that spiral nebulae were Galactic objects in the famous Shapley–Curtis debate. The angular rotation measured by Brunthaler et al. is ~ 1000 times smaller than van Maanen claimed, and, of course, consistent with an external galaxy (see **Figure 3**). Coupled with knowledge of the H I rotation speed and inclination of M33, the angular rotation rate yields a direct estimate of distance ("rotational parallax") of 730 ± 168 kpc, consistent with standard candle estimates. Significant improvement in the accuracy of this distance estimate can come from better H I data and a longer time baseline for the proper motion measurements.

Absolute proper motions (with respect to background quasars) have been measured for two Andromeda satellites: M33 and IC 10. Assuming these galaxies are gravitationally bound to Andromeda, their 3-dimensional motions yield a lower mass limit for Andromeda of $> 7.5 \times 10^{11}$ $M_\odot$ (Brunthaler et al. 2007). Of course, knowledge of the proper motion of Andromeda would refine this estimate and is key to unlocking the history and fate of the Local Group. Observations with the upgraded bandwidth of the VLBA and the Green Bank and Effelsberg 100-m telescopes are underway to measure the proper motion of M 31* (the weak AGN at the center of Andromeda) and the motions of a handful of H_2O masers recently discovered in the galaxy (Darling 2011). Awaiting a direct measurement of the absolute proper motion of Andromeda, one can use the fact that M33 has not been tidally disrupted by a close encounter with Andromeda in the past to place constraints on the

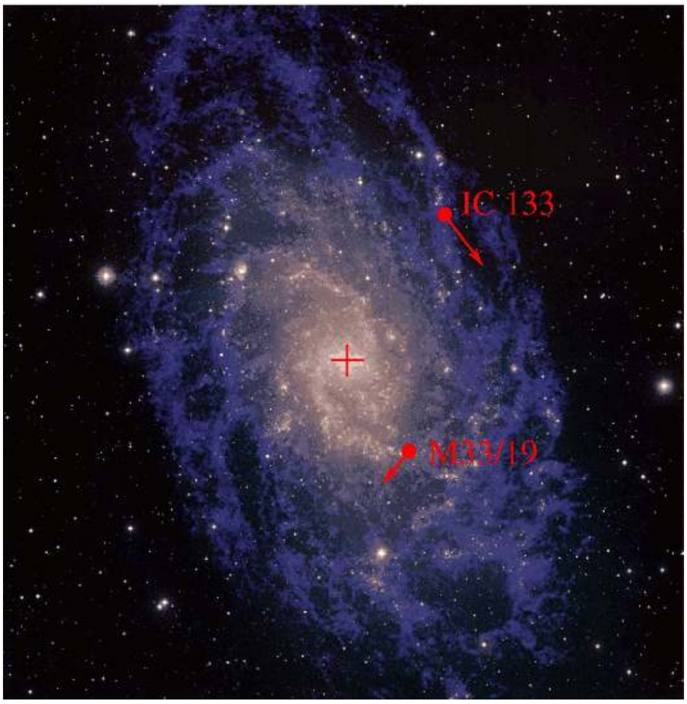

Figure 3:

Image of M 33, a satellite of the Andromeda galaxy, with the locations and measured proper motions of H_2O masers in two regions of massive star formation (Brunthaler et al. 2005). Both the relative motions (i.e., the van Maanen experiment) and the absolute motions with respect to a background quasar have been measured. The relative motions gives a "rotational parallax" distance, and the absolute motion can be used to constrain the mass of the Andromeda galaxy.

motion of Andromeda. In this way Loeb et al. (2005) showed that Andromeda likely has a proper motion of ~ 100 km s^{-1}.

2.11 Tests of General Relativity

The dominant uncertainty in modeling the Hulse-Taylor binary pulsar and measuring the effects of gravitational radiation on the binary orbit comes from uncertainty in the accelerations of the Sun ($\Theta_0{}^2/\mathrm{R}_0$) and the pulsar ($\Theta(R)^2/R$) as they orbit the center of the Galaxy (Damour & Taylor 1991). Using recently improved values for the fundamental Galactic parameters reduces the uncertainty in the binary orbital decay expected from gravitational radiation by nearly a factor of four compared to using the IAU recommended values (Reid et al. 2014). The dominant uncertainty in the general relativistic test parameter is now dominated by the uncertainty in the pulsar distance, and a VLBI parallax for the binary accurate to $\pm 14\%$ would bring the contribution from distance uncertainty down to that of Galactic parameter uncertainty.

Deller, Bailes & Tingay (2009a) obtained an accurate parallax distance of $1.15^{+0.22}_{-0.16}$ kpc for the pulsar binary J0737$-$3039 A/B. Given that these pulsars are only a kpc distant (not ~ 10 kpc as is the Hulse-Taylor pulsar), with this parallax accuracy uncertainties in the correction for the effects of Galactic accelerations are an order of magnitude smaller than for the Hulse-Taylor system. Thus, with perhaps another decade of pulsar timing, one might achieve a test of the effects of gravitational radiation predicted by general relativity at 0.01% level.

Pulsars orbiting the super-massive black hole at the Galactic center, Sgr A*, may show general relativistic effects that can be measured and tested based on high-accuracy astrometric observations. Pulsars near the Galactic center are strongly affected by interstellar scattering, which makes it difficult to observe these pulsars at $\lesssim 10$ GHz. For instance, the recently-discovered transient magnetar PSR J1745−2900 (Mori et al. 2013), located only 3" from Sgr A*, is highly likely to be in the Galactic center region. If another pulsar is found closer to Sgr A*, it could prove to be an excellent target for testing general relativity with unprecedented accuracy.

Gravity Probe B (GP-B) was a satellite mission to test general relativistic frame-dragging (Lense–Thirring effect) caused by the spin of the Earth. The satellite was equipped with four ultra-stable gyroscopes, allowing satellite altitude variation to be measured with unprecedented accuracy. Based on the data from the four gyroscopes spanning ~ 1 year, Everitt et al. (2011) reported a geodetic drift at -6601.8 ± 18.3 mas y^{-1} and a frame-dragging drift at -37.2 ± 7.2 mas y^{-1}. These results are fully consistent with the predictions of Einstein's theory of general relativity (-6606.1 mas y^{-1} and -39.2 mas y^{-1}, respectively). VLBI astrometry played a fundamental role in the calibration of the GP-B data. IM Peg (HR 8703), an RS CVn type binary system, was used as the reference star. Its parallax and proper motion were accurately measured with VLBA observations spanning 5 years (Shapiro et al. (2012) and references therein). Based on the astrometry of IM Peg relative to 3C454.3, the absolute proper motion of IM Peg was determined with an accuracy better than 0.1 mas y^{-1} (Ratner et al. 2012), which provided the fundamental basis for measuring the geodetic and frame dragging effect by GP-B.

The classical test of general relativity, measuring gravitational bending of star light by the Sun (Dyson, Eddington & Davidson 1919), has been repeated with radio interferometry by observing background radio sources and has provided one of the most accurate tests of general relativity. The most recent analysis of VLBI data reported that the post-Newtonian parameter γ is consistent with unity to an accuracy of one part in 10^{-4} (Lambert & Le Poncin-Lafitte 2009; Fomalont et al. 2009; Lambert & Le Poncin-Lafitte 2011). Additionally, Fomalont & Kopeikin (2003) detected the deflection of radio waves by Jupiter, including the retarded delay caused by Jupiter's motion, and claimed that this constrained the speed of gravitational waves, although this claim is controversial (see Asada (2002); Will (2003); Fomalont & Kopeikin (2009)).

2.12 Extrasolar Planets and Brown Dwarfs

A radio astrometric search for extrasolar planets was conducted by Lestrade et al. (1996) toward σ^2 CrB over a 7.5 year period. After removing the effects of parallax and proper motion, their post-fit residuals of < 0.3 mas excluded a Jupiter-mass planet orbiting at a radius of 4 AU from the central star. Guraido et al. (1997) observed the active K0 star AB Dor with the Australian LBA and, combined with HIPPARCOS data, inferred a companion with a mass of $\sim 0.1 M_\odot$. These studies demonstrate the potential of radio astrometry to detect low-mass companions, including brown dwarfs and planets.

Low-mass stars (< 1 $M_\odot$) could have habitable planets which are difficult to detect with optical radial-velocity techniques, because the stars are faint and activity can distort their line profiles, reducing the accuracy of velocity measurements. Thus, radio astrometric planet searches are complementary to other approaches. The Radio Interferometric Planet (RIPL) Search (Bower et al. 2009) and the Radio Interferometric Survey of Active Red Dwarfs (Gawroński, Goździewski & Katarzyński 2013) seek to detect the effects of planets around nearby low-mass stars, specifically active M dwarfs. For RIPL, the demonstrated astrometric accuracy is 260 μas, which for GJ 897A limits a planetary companion at 2 AU radius to < 0.15 M_J (Bower et al. 2011).

2.13 AGN Cores

Active Galactic Nuclei (AGNs) often show very strong and compact radio emission, with brightness temperatures up to and exceeding 10^{12} K. Bartel et al. (1986) measured the relative positions of a radio bright pair of QSOs, NRAO 512 and 3C 345, with a global VLBI network, revealing that the core positions of the sources were stable to within ± 20 μas y^{-1}. This stability corresponds to an upper limit of $\sim 1c$ for the core-motions, which is significantly lower than observed in the jets of super-luminal sources. Marcaide, Elosegui & Shapiro (1994), Rioja et al. (1997), Guirado et al. (1995) and Marti-Vidal et al. (2008) reported little if any relative proper motion between other QSO pairs (at levels of ~ 10 μas y^{-1}), consistent with contamination of stationary cores with some expanding plasma. Such studies point out a source of limiting "noise" when using radio loud QSOs for establishing fundamental reference frames.

In addition to measuring relative positions between two QSOs, one can precisely measure positions of jet components within a source at different frequencies. In this manner, Hada et al. (2011) measured the theoretically predicted core-shift as a function of observing frequency (Blandford & Königl 1979) for the super-massive black hole of M 87 (see **Figure 4**) and located the black hole relative to the jet emission with an accuracy of $\sim 10R_{\rm sch}$. Kovalev et al. (2008) and Sokolovsky et al. (2011) have confirmed that frequency-dependent core-shifts, such as observed in M 87, are common in large samples of AGNs with prominent jets. Bietenholz, Bartel & Rupen (2004) used SN 1993J in M 81 as a position reference for multifrequency imaging of M 81* (the AGN in that galaxy) to accurately locate the super-massive black hole. Later Marti-Vidal et al. (2011) found that the M 81* core position appears variable at lower frequencies, and they suggest this is a result of jet precession.

Porcas (2009) considered the effects of an AGN core-shifts on group-delay astrometry, used for measuring antenna locations for *geodetic* VLBI and for establishing reference frames (e.g., the ICRF). Usually group-delay measurements are conducted at 8.4 GHz and, to remove propagation delays in the ionosphere, simultaneous observations are also made at 2.3 GHz. When removing the dispersive component of delay to correct for ionospheric propagation delay, generally one assumes that AGN core positions are the same at the two observing frequencies. However, the core-shift effect on dual-frequency geodetic VLBI observations can be comparable to a position error of ~ 170 μas and should be measured and compensated for in the future, for example, when tying the radio reference frame with a new optical frame constructed by Gaia (Bourda et al. 2011).

2.14 Satellite Tracking

The technique of high-accuracy VLBI astrometry can be applied to locating spacecraft, using telemetry signals as radio beacons. In fact, astrometric observations of radio beacons placed on the moon by Apollo missions were among the earliest applications of phase-

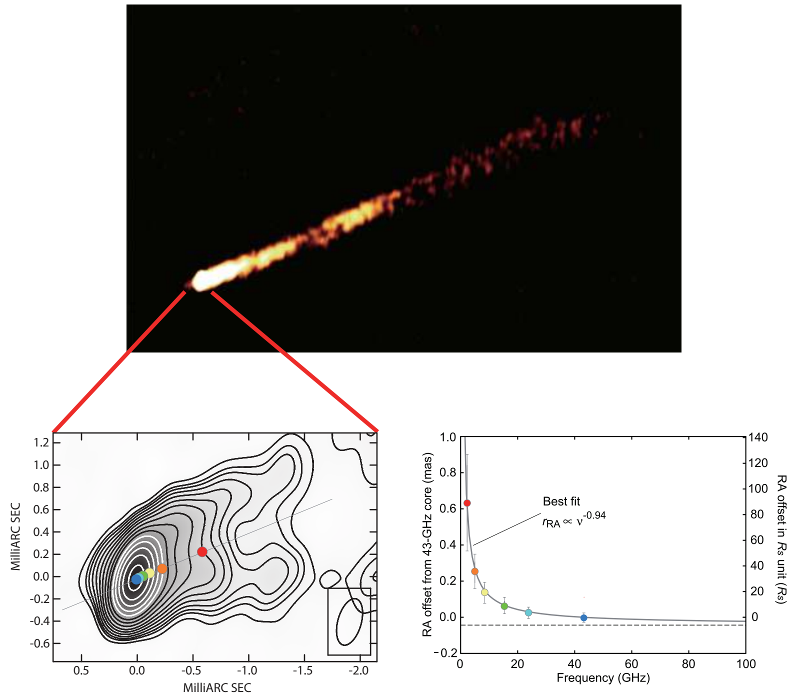

Figure 4:

The apparent shift in the core of M 87 as a function of observing frequency after Hada et al. (2012). This effect can be explained by frequency dependent optical depths and allows the position of the supermassive black hole to be accurately located on the images.

referencing VLBI. The Apollo Lunar Surface Experiments Package and Lunar Roving Vehicle radio transmitters from various Apollo missions spanned hundreds of km across the Lunar surface. These transmitters were observed by Counselman et al. (1973) and Salzberg (1973), who measured their separations with an accuracy of ∼ 1 m (∼ 0.5 mas). Later Slade et al. (1977) was able to tie these transmitters to the celestial reference frame with a positional accuracy of ∼1 mas. King, Counselman & Shapiro (1976) combined VLBI observations of Lunar transmitters with ranging data to better estimate the mass of the Earth-Moon system and the moment-of-inertia ratios of the moon. (See Lanyi, Bagri & Border (2007) for a recent review.)

Recently, high-accuracy radio astrometry played a part in generating a precise map of the Lunar gravity field in conjunction with the SELENE mission (Goossens et al. 2011). This was made possible by the high relative-position accuracy possible with in-beam astrometry (Kikuchi et al. 2009). This method was originally developed in 1990's for observing artificial radio sources near Venus (Border et al. 1992; Folkner et al. 1993) and made possible measurements of wind speed as a function of altitude, by monitoring the trajectories of probes released into the Venusian atmosphere (Counselman et al. 1979; Sagdeyev et al. 1992).

In the outer solar system, VLBI astrometry played a role in the PHOBOS-2 (Hildebrand et al. 1994) and Mars Odyssey missions (Antreasian et al. 2005). The motion of the Huygens probe as it descended in Titan's atmosphere revealed the vertical profile of its wind speed

Table 1: Major Radio Astrometric Interferometers

Array	Country/ region	Antenna diameters & number in array	Maximum baseline (km)	Operating frequencies	beam size (mas) comments
VLBA	USA	25m×10	8600 km	0.3–86 GHz	0.17 at 43 GHz
			homogeneous and best imaging capability		
VERA	Japan	20m×4	2300 km	6.7–43 GHz	0.63 at 43 GHz
			dedicated to astrometry with dual-beam system		
EVN	Europe	14m–100m, × ∼ 10	3000-10000 km	1.6–22 GHz	0.30 at 22 GHz
			high sensitivity with large dishes		
LBA	Australia	22m–70m, × ∼ 10	1700 km	1.4–22 GHz	1.7 at 22 GHz
			only VLBI array in the southern hemisphere		
JVLA	USA	25m×27	36 km	0.07–50 GHz	40 at 43 GHz
			connected array with high-sensitivity and excellent imaging		
ALMA	Chile	12m×54 + 7m×12	16 km	43–900 GHz	4.5 at 850 GHz
			large connected array at mm and sub-mm wavelengths		
SKA	Au/SA	∼1 km^2 aperture	∼ 3000 km	0.1–22 GHz	0.7 at 22 GHz
			future large cm-wavelength array		

(Witasse et al. 2006). The Cassini satellite itself was used to trace the gravity field of Saturn, and Jacobson et al. (2006) combined VLBI data with optical observations and Doppler ranging to better constrain the mass and potential of the Saturnian system. Also, VLBA observations of Cassini have measured the center-of-mass of the Saturnian system with an accuracy of 2 km (0.3 mas) with respect to the ICRF (Jones et al. 2011). The potential of radio astrometry for improving future space missions has been reviewed by Duev et al. (2012).

3 Arrays for Radio Astrometry

There are four major VLBI arrays that are regularly doing radio astrometry: the VLBA (Very Long Baseline Array) in US, the EVN (European VLBI Network), the VERA (VLBI Exploration of Radio Astrometry) array in Japan, and the LBA (Long Baseline Array) in Australia. Basic parameters of these arrays are summarized in **Table 1**.

The VLBA consists of ten 25-m diameter telescopes spread over US territory from Hawaii in the west to New Hampshire and Saint Croix in the east. With a maximum baseline length of ≈ 8000 km and frequency coverage from 300 MHz to 86 GHz, the VLBA is a flexible and sensitive array. The homogeneity of the array, with all the antennas and instruments identical, is advantageous as it makes calibration straightforward. While the VLBA is a general-purpose imaging array, recently phase-referencing astrometry has occupied a major portion of its observing time. Currently there are several large astrometric projects on the VLBA. The Bar and Spiral Structure Legacy (BeSSeL) Survey is measuring parallaxes and proper motions of hundreds of Galactic masers associated with high-mass star forming regions. The Gould's Belt Distances Survey aims to measure distances to and provide a detailed view of star-formation in the Solar neighborhood. The Radio Interferometric Planet Search (RIPL) is an astrometric search for planets around nearby low-mass stars. The Pleiades Distance Project seeks absolute parallaxes for up to 10 cluster stars in order to resolve the current cluster distance controversy and provide a solid foundation for many aspects of stellar astrophysics. Finally, the Megamaser Cosmology Project seeks to measure H_0 directly for 10 H_2O megamaser galaxies well into the Hubble flow in order to independently constrain H_0 with ±3% accuracy.

The VERA array consists of four 20-m diameter telescopes located across Japan with

Figure 5:

Schematic portrayal of the locations of the Very Long Baseline Array (VLBA) antennas. The VLBA has ten 25-m diameter antennas spanning the globe from Hawaii to New Hampshire and St. Croix.

a maximum baseline length of 2300 km (see **Figure 6**). Each antenna is equipped with two receiver systems that are independently steerable in the focal plane. As such VERA can observe target and reference sources simultaneously to effectively cancel tropospheric fluctuations. VERA is also the only array dedicated full-time to phase-referencing astrometry. Most of the observing time is spent on parallax measurements of maser sources tracing spiral structure in the Milky Way and of red giant stars.

The EVN array has antennas distributed across Europe as well as in other countries, including China, South Africa and USA. The EVN is most sensitive at frequencies < 10 GHz, owing to some large antennas: the Effelsberg 100-m, the Jodrell Bank 76-m and soon the Sardinia 64-m telescope. The array has been used for astrometric measurements of OH masers at 1.6 GHz, methanol masers at 6.7 GHz, and active stars.

The LBA in Australia is the only VLBI array regularly operating in the southern hemisphere. It has high sensitivity when the Parkes 64-m and Tidbinbilla 70-m telescopes are included. The LBA has provided astrometric measurements for southern pulsars, and hopefully it will soon be used for maser parallaxes. This is necessary in order to trace the 3-dimensional structure of the roughly one-third of the Milky Way that cannot be observed from the north.

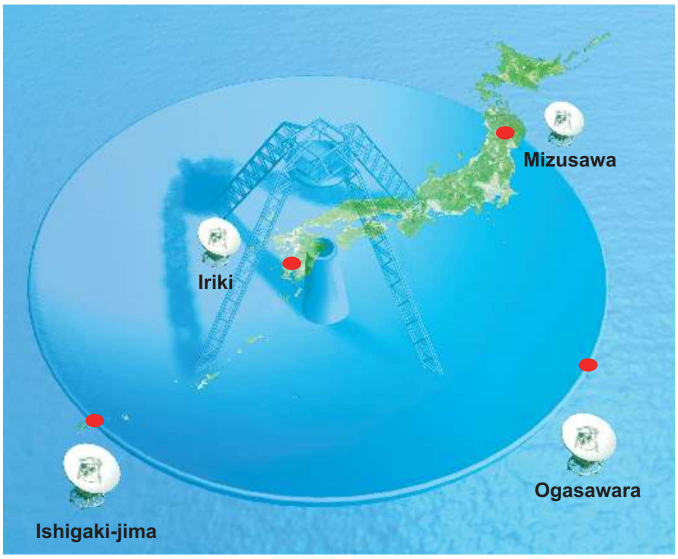

Figure 6:

Schematic portrayal of the locations of the VERA antennas. The VERA array has four 20-m diameter antennas spanning the Japan and is dedicated to astrometric observations.

4 Fundamentals of Radio Astrometry

The fundamental observable for a radio interferometer is the arrival time difference of wavefronts between antennas, owing to the finite propagation speed of electro-magnetic waves (the speed of light c). For an ideal interferometer, the arrival time difference is determined by the locations of the antennas with respect to the line-of-sight to the source and is referred to as the "geometric delay." The basic equation of a radio interferometer, which relates the geometric delay, τ_g, to the source unit vector, $\vec{s}$, and the baseline vector, $\vec{B}$, is given by

$$\tau_g = \frac{\vec{s} \cdot \vec{B}}{c} \quad . \tag{1}$$

In **Figure 7**, we sketch the geometry of these vectors. Note that while the source vector $\vec{s}$ has two parameters (e.g., right ascension and declination), the geometric delay is a scalar and so multiple measurements of geometric delays are required to solve for a source position. Such measurements can be made, even with a single baseline, by utilizing the Earth's rotation, which changes the orientation of the baseline vector with respect to the celestial frame.

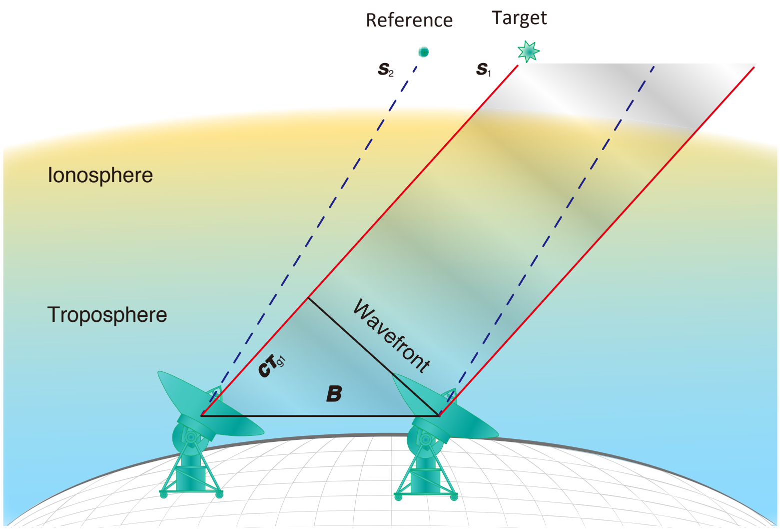

Figure 7:

Schematic view of a delay measurement in phase-referencing astrometry. Here, for simplicity, an array with two stations is shown. The baseline vector and source directions are indicated by lines. In relative astrometry, the target and adjacent reference sources are observed (nearly) at the same time so delay errors can be effectively canceled in the relative measurement. For relative radio astrometry, the dominant error sources are generally uncompensated propagation delays in troposphere and/or ionosphere.

We now consider the effects of observational errors on astrometric accuracy. Given the uncertainty in a delay measurement, which we denote $\Delta\tau$, from Equation 1 one can roughly estimate the astrometric error, Δs:

$$\Delta s \approx \frac{c\Delta\tau}{|B|} \quad . \tag{2}$$

As seen in Equation 2, for a given $\Delta\tau$, astrometric accuracy improves with longer baselines. This is the fundamental reason why VLBI, which utilizes continental and/or intercontinental baselines, can achieve the highest accuracy astrometry. For example, for an 8,000 km baseline and a typical delay error of $\sim$2 cm (converted to path length by $c\Delta\tau$), one expects an astrometric error of ~ 0.5 mas. This is a typical error for *absolute* astrometry, such as measuring QSO positions in the ICRF using broad-band delay measurements.

For Galaxy-scale parallaxes, however, this accuracy is insufficient as parallaxes can be ~ 0.1 mas, corresponding to distances of ~ 10 kpc. At such distances, one needs astrometric accuracy of ± 10 μas to achieve $\pm 10\%$ uncertainty. In order to obtain μas-level accuracy, one must substantially cancel systematic delay errors through *relative* astrometry, i.e., a position measurement with respect to a nearby reference source. Historically, the concept of relative astrometry has been attributed to Galileo, who proposed measuring the parallax of a nearby star with respect to a more distant star located close by on the sky.

4.1 Relative Astrometry

The delay measured with an interferometer can be considered as the sum of the geometric delay (which we would like to know) and additional terms (which need to removed from the data):

$$\tau_{\text{obs}} = \tau_{\text{g}} + \tau_{\text{tropo}} + \tau_{\text{iono}} + \tau_{\text{ant}} + \tau_{\text{inst}} + \tau_{\text{struc}} + \tau_{\text{therm}} \quad . \tag{3}$$

Here τ_{tropo} and τ_{iono} are the delays in the propagation of the signal through the troposphere and ionosphere, respectively, τ_{ant} is caused by an error in the location of an antenna, τ_{inst} is an instrumental delay in the telescope or electronics, τ_{struc} is the delay due to unmodeled source structure, and τ_{therm} is the uncertainty in measuring delay caused by thermal noise. Note that generally throughout this review the terms "delay" and "phase" (or phase-delay) can be used interchangeably: for instance, the interferometric phase caused by the geometric delay in Equation 1 can be written as,

$$\phi_{\text{g}} = 2\pi\nu\tau_{\text{g}} \quad , \tag{4}$$

where ν is the observing frequency.

For relative astrometry, one observes two sources, the target and reference, at nearly the same time and nearly the same position on the sky, and differences the observed delays (phases) between the pair of sources. This type of observation is often referred to as "phase-referencing," as the observed phase of the reference source is used to correct the phase of the target. Applying Equation 3 for the difference between two sources, we obtain the delay difference observable:

$$\begin{aligned} \Delta\tau_{\text{obs}} &= (\tau_{\text{geo},1} - \tau_{\text{geo},2}) \\ &+ (\tau_{\text{tropo},1} - \tau_{\text{tropo},2}) + (\tau_{\text{iono},1} - \tau_{\text{iono},2}) \\ &+ (\tau_{\text{ant},1} - \tau_{\text{ant},2}) + (\tau_{\text{inst},1} - \tau_{\text{inst},2}) \\ &+ (\tau_{\text{struc},1} - \tau_{\text{struc},2}) + (\tau_{\text{therm},1} - \tau_{\text{therm},2}) \quad . \end{aligned} \tag{5}$$

Here subscripts 1 and 2 denote the quantities for the target and reference source, respectively. The first term is the difference in geometric delay between the source and reference, which corresponds to the relative position of the target source with respect to the reference source. The additional terms in the Equation 5 may be reduced if they are similar for the two lines of sight. As will be discussed in detail later, four terms (τ_{trop}, τ_{iono}, τ_{star}, and τ_{inst}) are antenna-based quantities (delays originated at each antenna) and generally are similar for the target and reference lines of sight, for small source separations.

Antenna-based terms can be effectively reduced by phase-referencing. For example, the delay error generated by an antenna position offset, $\Delta\vec{B}$, is given by

$$\tau_{\text{ant}} = \frac{\vec{s}\cdot\Delta\vec{B}}{c} \sim \frac{|\Delta B|}{c} \quad . \tag{6}$$

Note the approximation used to obtain the right hand side of Equation 6 is that the trigonometric terms in the vector dot product are generally $\lesssim 1$. Differencing the antenna delays for two adjacent sources, yields

$$\Delta\tau_{\text{ant}} = (\tau_{\text{ant},1} - \tau_{\text{ant},2}) = \frac{(\vec{s_1} - \vec{s_2})\cdot\Delta\vec{B}}{c} \sim \theta_{\text{sep}}\frac{|\Delta B|}{c} \quad , \tag{7}$$

where θ_{sep} is the separation angle between the sources. Comparison of Equations 6 and 7 shows that the delay error caused by an antenna position error is reduced by a factor of

$\theta_{\rm sep}$ in the differenced delay. This reduction can significantly improve *relative* over *absolute* astrometric accuracy. For a separation of $\theta_{\rm sep} = 1^\circ$, the error reduction factor ($\theta_{\rm sep}$) is about 0.02 (radians).

As we will discuss later in more detail, the dominant error source in radio astrometry is uncompensated propagation delays, generally tropospheric for observing frequencies $\gtrsim$ 10 GHz and ionosphere for lower frequencies. These terms are "antenna-based," just as the antenna location errors described above. A rough estimate of astrometric accuracy achievable in the presence of propagation delay errors is given by

$$\Delta s_{\rm rel} \approx \theta_{\rm sep} \frac{c\Delta\tau}{|B|} \quad . \tag{8}$$

The reduction in position uncertainty in going from Equation 2 to Equation 8 is, of course, the addition of the canceling term, $\theta_{\rm sep}$. Using the same example values previously used for absolute astrometry, ($|B|$=8000 km and a delay error of $c\Delta t \sim 2$ cm), relative astrometric accuracy for a 1° source separation is ~ 10 μas.

4.2 Sources of Delay Error

Uncompensated delay differences between antennas in an interferometric array usually limit radio astrometric accuracy. In this subsection, we discuss sources of delay errors individually.

4.2.1 Troposphere

The propagation speed of electro-magnetic waves in the troposphere is slower than in vacuum, causing an extra delay (τ_{tropo}) to be added to the geometric delay. The tropospheric delay is almost entirely non-dispersive (frequency independent) at radio frequencies. It is convenient to separate the tropospheric delay into two components based on the timescales of fluctuation: a slowly ($\sim$ hours) and rapidly ($\sim$ minutes) varying term.

The rapidly varying term is associated with the passage of small "clouds" of water vapor flowing at wind speeds of ~ 10 m s^{-1} at a characteristic height of ~ 1 km over each antenna. This can be the main cause of coherence loss in interferometric observations. The characteristic time scales for interferometer phase fluctuations induced by tropospheric water vapor can be described by the Allan standard deviation ($\sigma_{\rm A}$) and is typically $\sim$ 0.5 to 1×10^{-13} over timescales of 1 to 100 sec (Thompson, Moran & Swenson 2001; Honma et al. 2003). An interferometer coherence time, $\tau_{\rm coh}$, can be defined as the time interval over which phase fluctuation differences between two antennas accumulate one radian. At an observing frequency ν, this implies

$$2\pi\sigma_{\rm A}\nu\tau_{\rm coh} \sim 1 \quad . \tag{9}$$

For $\sigma_{\rm A} = 0.7 \times 10^{-13}$ and $\nu = 22$ GHz, this implies a coherence time of ~ 100 sec. One must measure and remove the phase variations on a time-scale shorter than the coherence time. Rapid switching between the target and calibrator sources can usually accomplish this, provided the antennas can slew and settle on sources rapidly (see §4.3).

The rapid variations from tropospheric delays can be completely removed if one can simultaneously observe the target and calibrate sources . This is done with the VERA antennas, which have dual-beam observing systems. Alternatively, this can also be accomplished if one is fortunate in finding a source pair with a very small angular separation, so that both fit within the primary beam of the antennas ("in-beam" calibration). Note that with either method, this still leaves a spatial variation component, but that term is generally smaller than the temporal term for source separations of a few degrees.

The slowly varying delay term is generally associated with the "dry" part of the troposphere, although the slow term can also contain a small, relatively stable contribution from water vapor. At sea-level, a typical path delay for the dry component is 230 cm at the zenith and water vapor can contribute up to a several tens of cm for very humid locations. The total dry delay can be estimated from antenna latitude and elevation, and if necessary using local temperature and pressure values. Since the total dry delay is considerable, it is important to remove its effects during correlation, or early in post-correlation processing, by carefully accounting for the exact slant path through the atmosphere (air mass), which will be different for the target and calibrator. The slowly varying wet component cannot reliably be estimated from surface weather parameters and needs to be directly measured and removed to achieve μas astrometry (see §5.1.1 and §5.1.2 for details).

4.2.2 Ionospheric delay The ionosphere is a partially ionized layer located between ~ 50 and ~ 500 km altitude. An electromagnetic wave propagating through this plasma experiences phase and group delays that are frequency dependent (i.e., dispersive delays). The phase and group delay are given by

$$\tau_{\rm iono} \equiv \frac{1}{2\pi}\frac{\phi}{\nu} = -\frac{cr_0}{2\pi\nu^2} I_e \quad , \tag{10}$$

and

$$\tau_{\rm grp,iono} \equiv \frac{1}{2\pi}\frac{\partial\phi}{\partial\nu} = \frac{cr_0}{2\pi\nu^2} I_e = -\tau_{\rm iono} \quad , \tag{11}$$

where r_0 is the classical electron radius and $I_e = \int n_e dl$ is the electron column density along the line of sight or total electron content (TEC). Due to the dispersive nature of plasma, delays are larger at lower frequency because of the ν^{-2} dependence. (Note that the ionospheric phase delay has the opposite sign of the group delay; therefore correction of interferometer phase for ionospheric delays is different than for tropospheric delays.)

The ionization of the ionosphere is predominantly from solar radiation, and thus there is a strong diurnal variation, as well as from the 11 year solar cycle. Due to the diurnal variation, the ionospheric delay needs to be modeled (or measured) and calibrated on hour scales. Modeling of the ionospheric delays is done by a combination of a vertical TEC (VTEC) and a mapping (air mass like) function. Typical values for VTEC range from a few to 100 TECU, where 1 TECU corresponds to an electron column density of 10^{16} m^{-2}. Once the TEC toward a source is known, the ionospheric delay (in path length units) can be calculated by the following relation,

$$|c\tau_{\rm iono}| = 40.3 \left(\frac{I_e}{\rm TECU}\right)\left(\frac{\nu}{\rm GHz}\right)^{-2} \quad ({\rm cm}) \quad . \tag{12}$$

At a frequency of 22 GHz, a 50 TECU column density causes a delay equivalent to an extra path length of ~ 4 cm, but it reaches ~ 400 cm at a frequency of 2 GHz.

Because of the dispersive nature of the ionospheric delay, dual-frequency observations are effective for calibration. Most geodetic measurements involve simultaneous observations at 2.3 and 8.4 GHz in order to calculate and then remove ionospheric delays. Another way to measure ionospheric TEC values is to use GPS data, which provide dual-frequency signals at 1.23 and 1.58 GHz. Several services accumulate GPS data from stations around the Earth and provide global TEC models approximately every two hours. Generally, radio interferometric data are calibrated for ionospheric delays using these models.

4.2.3 Instrumental Delay Radio propagation in antenna structures, feeds, and electronics causes additional delays, which we lump together as "instrumental delays" (τ_{inst}). In addition, there are electronic phase offsets associated with the generation of the local oscillators used to mix the observed frequencies to "intermediate" frequencies (~ 1 GHz) prior to correlation. The data recorded at each antenna are time-tagged using a clock tied to the fundamental frequency standard at each station (usually a hydrogen maser atomic oscillator), and owing to slight frequency offsets (that do not affect local oscillator stability) these clocks generally gain or lose time at a rate of one part in $\sim 10^{-14}$ (only ~ 1 nsec per day!). However, a delay error of 1 nsec causes a phase slope of π radians across a 500 MHz observational bandwidth, and it is critical to correct for this. Calibration observations using "geodetic blocks" (see §5.1.1) can remove clock errors to an accuracy of $\lesssim 0.1$ nsec. Other instrumental delay and phase offsets are generally relatively slowly varying, for well designed systems and temperature controlled electronics, and can be calibrated and removed by observations of strong sources a few times a day.

Any residual instrumental delay and phase offsets will be mostly canceled when switching between two sources, provided the electronics are not changed. Note that if one of the sources is a spectral line and the other a continuum emitter, one should try to place the line near the center of the continuum band to ensure better calibration. On the other hand, if the two sources are observed with different receivers, which is the case for dual-beam receiving at VERA, there is a need for additional calibration of the instrumental delay and phase, such as by using an artificial noise source (see §4.3).

4.2.4 Antenna Position The antenna position is usually defined as the intersection of azimuth and elevation axes and can be measured to an accuracy of $\lesssim 3$ mm with regular geodetic observations. The Earth's rotation rate varies (measured as a time correction, UT1−UTC) as does the location of an antenna on the Earth's crust with respect to its spin axis (polar motion). Together these are called Earth Orientation Parameters (EOP). EOP values are determined on a daily basis by the International Earth Rotation and Reference Systems Service (IERS) by utilizing global GPS data and geodetic VLBI observations. A typical error in EOP values is ≈ 0.1 mas, provided the final (not preliminary or extrapolated) values are used. With high accuracy antenna locations and EOP corrections, the total uncertainty in the position of an antenna contributes less to the astrometric error budget than uncertainty in atmospheric propagation delays.

4.2.5 Source Structure If the observed sources are not point like, interferometric delay/phase can be affected by source structure. Since structure phase shifts are independent for the target and reference sources, their effects do not cancel when differencing the phases in relative astrometry. Source structure phases are baseline-based quantities. Because there are $\sim N^2$ baselines for N antennas in an array, structure phase can be separated from station-based quantities and estimated using self-calibration (closure techniques and hybrid-mapping). Once a source image is obtained, phase shifts caused by source structure can be calculated and subtracted from observed interferometric data. Note that since self-calibration loses absolute position information, if one self-calibrates the reference source data, one must apply the *same* calibrations to both the reference and target source to preserve relative astrometric accuracy. Generally it is not a good idea to self-calibrate the target source data, but instead measure the structure in the phase-referenced images.

4.2.6 Thermal noise

Thermal (usually dominated by receiver) noise is random and cannot be calibrated and removed. However, a random process does not cause systematic offsets, and by integrating over many samples its effects can be reduced. Thermal noise in an interferometric image leads to position measurement uncertainty given by Equation 1 of Reid et al. (1988):

$$\Delta\theta_{\rm therm} \approx 0.5\frac{\theta_{\rm beam}}{SNR} \approx 0.5\frac{\lambda}{B}\frac{1}{SNR} \quad . \tag{13}$$

For a baseline length $B = 8000$ km and observing wavelength $\lambda = 1.3$ cm, the synthesized beam (FWHM) size is $\theta_{\rm beam} \approx 0.3$ mas. Thus, for a source with an image signal-to-noise ratio $SNR \sim 30$, the expected position error due to thermal noise is only ≈ 5 μas. Therefore, thermal noise often is not a major source of radio astrometric error.

4.3 Observing methods

Several methods of phase-referencing are commonly used: source switching, dual-beam, and in-beam observations. Source switching or "nodding" is the most-commonly used observing method, because it does not require a special radio telescope and can be used for all source pairs. The only requirement is that slewing/settling times are short enough to track tropospheric phase fluctuations. As discussed in §4.2.1, coherence times at an observing frequency of 22 GHz are ~ 100 sec. Therefore switching cycles should be shorter than this time, e.g., a cycle of 60 sec obtained by integrating for 20 sec on the reference, 10 sec for slewing to the target, integrating for 20 sec on the target, then 10 sec for slewing back to the reference. Because of the non-dispersive nature of tropospheric delays, the interferometer coherence time scales linearly with wavelength, i.e., $\tau_{\rm coh} \propto \lambda$. Hence at a short wavelengths, the coherence time can be problematic. For an observing wavelength of $\lambda = 1.3$ mm ($\nu = 230$ GHz), the coherence time is likely to be ~ 10 sec. This makes it practically impossible to conduct switched VLBI observations at $\lesssim 1$ mm wavelength.

In dual-beam observations, two sources are observed simultaneously using independent feeds and receivers. This can be done using multi-feed systems on a single antenna, as with VERA, or with multiple antennas at each site (Rioja et al. 2009; Broderick, Loeb & Reid 2011). There is no gap between the observations of the target and reference sources, and hence there is no coherence loss owing to temporal phase fluctuations. The antennas of the VERA array achieve this with two receivers installed at the Cassegrain focus. These receivers are independently steerable with a Steward-mount platform, and one can observe a source pair with separation angles between 0.3° to 2.2°. In dual-beam radio astrometry, special care needs to be taken to calibrate the instrumental delay, because it is not common to the target and reference source and thus will not cancel when phase-referencing.

In-beam observations can be regarded as a special case of phase-referencing, where the target and reference sources are so closely located that the two sources can be observed simultaneously with a single feed (within the primary beam of each antenna). In such a case, calibration error can be very effectively reduced, because the observations are done at the same time for the target and reference, and, because the separation angle is small, most systematic errors are largely canceled. However, finding a sufficiently strong reference source may be difficult; as such in-beam observations are more common at lower observing frequencies, as the primary beam becomes larger and the reference sources stronger.

5 Advanced Techniques

For parameters typical of cm-wavelength VLBI observations seeking to measure relative positions between two sources separated by $\approx 1^\circ$ with ≈ 10 μas accuracy, phase reference sources should have coordinates known to $\lesssim 5$ mas, antenna locations known to $\lesssim 1$ cm, and electronic, clock and propagation delays known to $\lesssim 0.05$ nsec.

5.1 Tropospheric Delay Calibration

Tropospheric (non-dispersive) delays are usually calibrated by one of two methods: 1) using geodetic-like observing blocks or 2) using GPS data.

5.1.1 Geodetic Block Calibration:

One can use observations of radio sources spread over the sky to measure broad-band (group) delays. For sources with positions known to better than ≈ 1 mas, group delay residuals will generally be dominated by the effects of tropospheric (and at low frequencies ionospheric) mis-modeling, provided the geometric model for the array is accurate to better than ± 1 cm (including antenna locations, earth orientation parameters and solid-earth tides). By observing ≈ 10 sources over a range of source azimuths and, most importantly, elevations in rapid succession ($\lesssim 30$ min), one can estimate residual "zenith" tropospheric delays at each telescope. These observing blocks are similar to those used for geodetic VLBI observations to determine source and telescope positions, as well as Earth's orientation parameters and, hence, are called "geodetic blocks."

The observing sequence can be determined by Monte Carlo simulations of large numbers of blocks and choosing the block with the lowest expected zenith-delay uncertainties. Operationally, it may be best to choose sources above an elevation of $\approx 8^\circ$ and available at a minimum of about $\sim 60\%$ of the telescopes in the array. Geodetic blocks should be placed before the start, during (roughly every 2 hours), and at the end of phase-reference observations. This allows one to monitor slow changes in the total tropospheric delay for each telescope. In order to measure group delays accurately, the observations should span the maximum IF bandwidth, spaced in a "minimum redundancy pattern" to uniformly sample, as best as possible, all frequency differences. For a system with 8 IF bands, this can be accomplished with bands spaced by 0, 1, 4, 9, 15, 22, 32 and 34 units. If the recording system limited to 500 MHz IF bandwidth, the unit separation would be ≈ 14.7 MHz. With such a setup, estimated zenith delays are generally accurate to ≈ 0.03 nsec (≈ 1 cm of propagation path-delay). Comparisons of the geodetic block technique with those using Global Positioning System (GPS) data and an image-optimization approach confirm this accuracy (Honma, Tamura & Reid 2008).

Residual multi-band (group) delays and fringe rates are modeled as owing to a vertical tropospheric delay and delay-rate, as well as a clock offset and clock drift rate, at each antenna. Note that the geodetic blocks need not be observed at the same frequency as the phase-referencing observations. If one has independent calibration of ionospheric (dispersive) delays (see §5.2), then it is simplest to observe the geodetic blocks at a frequency (ν) above ≈ 20 GHz to avoid contamination of the group delays by residual ionospheric effects, which decline approximately as $1/\nu^2$. However, if one is limited to one (wide-band) receiver, then for observing frequencies below about ≈ 10 GHz, it is important to remove unmodeled ionospheric contributions to the geodetic group delays, since correction of interferometer phases has a different sign for dispersive compared to non-dispersive delays. This can be accomplished with "dual-frequency" geodetic blocks as outlined in §5.2.

5.1.2 GPS Tropospheric Delay Calibration:

The GPS is a navigation system used to determine an accurate three-dimensional position for an observer on the Earth. The system consists of more than 20 satellites constituting an artificial "constellation" of reference sources. Accurate positions of the satellites are broadcast by radio transmission to receivers on Earth. The basic principles for position determination using GPS signals is similar to geodetic VLBI: the receiver position can be accurately determined based on delay measurements from multiple satellites. Since the broadcasts are at low frequencies (1.2 to 1.6 GHz), propagation delays in the ionosphere strongly affect the data. Dual frequencies allow removal of the ionospheric (dispersive) delay, and by observing several GPS satellites at different slant-paths through the atmosphere simultaneously, one can solve for the tropospheric delay as well as the receiver position. As such, one can use GPS data to calibrate tropospheric delays. Steigenberger et al. (2007) and Honma, Tamura & Reid (2008) have conducted detailed comparisons of tropospheric delay measurements by GPS and geodetic-mode VLBI (see §5.1.1) observations; both studies conclude that the difference between the two methods are small, $\lesssim 2$ cm, with no systematic differences.

5.2 Ionospheric Delay Calibration

In principle, the effects of ionospheric (dispersive) delays can be largely removed by using global models of the total electron content (Walker & Chatterjee 2000), by direct use of GPS data at each antenna, or from dual-frequency geodetic block observations. Because the ionosphere is confined to a shell far above the Earth's surface, rays from the source to a telescope can penetrate the ionosphere far from the telescope location on the Earth's surface. This generally favors using global models, based on smoothed results from a grid of GPS stations, over measurements made only at the VLBI telescopes. However, this is an area of current development and the methods of dispersive delay calibration may improve.

If one observes at frequencies below ≈ 10 GHz, one can in principle obtain both dispersive and non-dispersive delays simultaneously from "wide-band" geodetic blocks. For example, with receivers covering 4 to 8 GHz, one can generate two separate sets of geodetic block data: spanning 500 MHz centered at the low end of the band ($\nu_L = 4.25$ GHz) and at the high end of the band ($\nu_H = 7.75$ GHz). This gives observables $\tau(\nu_L)$ and $\tau(\nu_H)$, which contain both dispersive and non-dispersive delays (eg, tropospheric delays and clock terms). Differencing $\tau(\nu_L)$ and $\tau(\nu_H)$ values for all sources and baselines yields the dispersive contribution. The dispersive contribution can be used to model the ionospheric contribution and, importantly, can be scaled and subtracted from the $\tau(\nu_H)$ delays to produce pure non-dispersive delays. The non-dispersive delays can then be modeled as described in §4.2.1 to solve for pure tropospheric and clock terms. Note, that if one uses observations of a strong continuum source (fringe finder) to remove electronic delay differences among IF sub-bands (i.e., zeroing the delay on the fringe finder scan), this must be taken into account when modeling the dispersive delays.

An alternative to direct measurement is to use global maps of total ionospheric electron content generated from GPS data. Global Ionosphere Maps (GIMs) are produced on a regular basis by several groups, such as NASA, EAS, CODE, and UCP, who provide GIMs every two hours. Basic trends in these global maps are generally consistent with each other, although there are differences in scale for TEC values. Also note that currently GIMs have a typical angular resolution of 2.5 deg, and thus small scale fluctuations in the ionosphere may not be well traced. Hernández-Pajares et al. (2009) compared TEC values obtained by GPS and direct measurements (such as with JASON and TOPEX) and found vertical

TEC values among the methods differ at the $\approx 20\%$ level. For a 50 TECU zenith column and an error of $\pm 20\%$, the uncertainty in the ionospheric delay correction would be ~ 1 cm at an observing frequency of 22 GHz, which is slightly smaller than the delay error caused by the troposphere. On the other hand, at frequencies below 10 GHz the ionosphere is the dominant contributor to the delay error budget, even after corrections with GIMs are applied.

5.3 Dual-beam Systems

For a dual-beam receiving system, an additional calibration is required, because the propagation paths through the antenna and electronics are independent for the target and reference sources. At VERA, the horn-on-dish method is utilized (Honma et al. 2008a), in which an artificial noise source is mounted on an antenna's main reflector and a common signal is injected into both receivers. During observations, cross-correlation of the noise source between the two receivers is monitored in real-time, so that one can trace the time variation of the instrumental delay difference. The measured delay difference between the two receivers can be applied in post-processing. Honma et al. (2008a) have conducted tests of the horn-on-dish calibration and found that the VERA system can measure instrumental (path) delay differences to an accuracy of ± 0.1 mm, more than adequate for 10 μas relative astrometry.

5.4 Reference Source Position

The error in the position of the source used as the phase reference causes an error in its delay/phase measurements, and these errors are then propagated to the target source. The effect of a reference source position offset differs from other errors previously discussed. The first order effect is that the position offset of the reference source is transferred to the target source position. If the reference source has negligible proper motion and parallax, this only introduces a constant term, which is absorbed when fitting for parallax and proper motion. This is why we do not include such a term in Equation (3).

However, if the reference source position offset becomes large ($\gtrsim 10$ mas), there are additional second-order effects which come from the fact that the target and reference sources are separated on the sky. Because they are at different positions, the interferometer phase response to a position offset at one position on the sky does not exactly mimic the response at the other position. These second order effects lead to a small position error and to degraded image quality. For an interferometric fringe spacing of 1 mas and a pair separation of 1°, one radian of second order phase-shift results from a calibrator position offset of ~ 10 mas (this offset, δ_θ, can be estimated by $2\pi\theta_{\rm sep}(\delta_\theta/\theta_{\rm beam}) \sim 1$). In general, for phase-referencing astrometry, one needs to know the calibrator position with an accuracy of $\lesssim 10$ mas. For a finer beam size or larger separation angle, the required positional accuracy is even higher.

There are several methods for determining the absolute position of a phase reference source. If one can find a compact ICRF radio source (with $\delta_\theta \approx 1$ mas) close to the target source, one can transfer the position accuracy to the phase-reference source. However, ICRF sources are sparsely distributed on the sky and some are heavily resolved on long interferometer baselines. In such cases, one should include an ICRF source in the phase-referenced observations, even if offset by up to about $\approx 5^\circ$ from the other sources used for differential astrometry, in order to determine their positions. Even if using a distant ICRF source as a reference produces poor images for other sources, one can usually obtain ~ 1 mas accurate positions (and then discard the ICRF source data).

Alternatively, one can do preparatory observations to measure the position of a phase reference source. Usually connected-element interferometers (e.g., JVLA, eMERLIN, or the ATCA), which are limited in baseline length to $\lesssim 100$ km, can yield absolute positions with accuracies between 0.01 and 1 arcsec. While this is usually adequate for VLBI data correlation, it is not good enough for high accuracy VLBI astrometry. Instead, VLBI observations using broad-band group-delay observables (as done for ICRF campaigns) are preferable.

If a maser source is to serve as the phase reference, then broad-band group-delays cannot be measured, since spectral lines are intrinsically very narrow, leading to large uncertainty in group-delay estimates. In this case, it is best to use an ICRF source to transfer positional accuracy via phase-referencing. As a last resort, if no qualified source is available, one can attempt to synthesize a maser spot image *without* phase-referencing. If the VLBI data have been correlated (or later corrected) with a model accurate to a few wavelengths of path delay, then such an image will resemble optical speckles (caused by short-term phase fluctuations induced by tropospheric water fluctuations and instabilities in the frequency standard). However, the centroid of these speckles can often be determined to ~ 10 mas, which may be sufficient for the position of the phase reference.

5.5 Source Elevation Limits

Often the dominant source of systematic error is uncompensated tropospheric delays. At any telescope, if one misestimates the zenith (i.e., $z = 0$) tropospheric delay by $\delta\tau_0$, this error is magnified at larger zenith angles by a factor of $\approx \sec z$. The differential effect between the target and a background source, with a zenith angle difference of Δz, is then given by $\Delta\tau(z) = \delta\tau_0 \frac{\partial \sec z}{\partial z} \Delta z = \delta\tau_0 \sec z \tan z \Delta z$. Note that $\Delta\tau(z)$ increases dramatically at large zenith angles where both $\sec z$ and $\tan z$ tend to diverge. For example, the ratio of differential delay error $\Delta\tau(z)$ at $z = 70^\circ$ to $z = 45^\circ$ is a factor of 8.0. This suggests that astrometric observations should be limited, whenever possible, to small zenith angles. Of course, when restricting observations to small zenith angles, one must balance the loss of interferometer (u, v)-coverage, which affects both sensitivity and image fidelity, against increasing systematic errors that come with large zenith angle observations. In practice, it may prove valuable to fully simulate interferometric observations in order to estimate an optimum zenith angle limit for the declination of a given target source and the orientation and separation on the sky of the background source.

5.6 Measuring Positions

Perhaps the simplest method of measuring a position from radio interferometric data is to work in the image domain. This involves placing the visibility (u, v) data on a grid, performing a 2-dimensional Fourier transformation to sky coordinates, $(u, v) \rightarrow (x, y)$, deconvolving the resulting "dirty" map using the "dirty" beam (point source response) with the CLEAN algorithm, and fitting a 2-dimensional Gaussian brightness distribution to compact emission components. This provides offsets, $(\Delta x, \Delta y)$, from the map center, whose absolute position is defined by the position used when cross-correlating the interferometer data and any subsequent shifts applied during calibration.

Care must be taken in both shifting positions and interpreting the measured offsets from the map center, to properly account for the effects of precession, nutation, aberration and even general relativistic ray bending near the Sun. For example, position shifts applied to (u, v)-data are best done by calculating the full interferometric delay and phase for the desired source position and subtracting those values for the original (correlator) position. Simply calculating a differential correction can lead to significant astrometric errors. Similarly, one should not simply add map offsets, $(\Delta x, \Delta y)$ (which "know nothing" of physical effects) to the map-center coordinates, without correcting for differential precession, nutation, and aberration, unless the map offsets are very small. For example, over time scales of less than a few years, neglecting differential effects generally leads to position errors of $\sim 10^{-4}(\Delta x, \Delta y)$. So, to ensure astrometric accuracies of ~ 1 μas, $(\Delta x, \Delta y)$ values should be $\lesssim 10$ mas. Therefore, if one measures large $(\Delta x, \Delta y)$ values in a map, one should (accurately) shift positions in the (u, v)-data, re-image, and re-measure the offsets.

6 Future

6.1 Space VLBI

Space-VLBI involves using a radio antenna in orbit around the Earth to obtain baselines lengths greater than an Earth diameter. As is clear from Equation 2, for fixed delay uncertainty one gains astrometric accuracy as the baseline length increases. For space VLBI to improve on Earth-based astrometry, the satellite position (orbit determination) must be determined to ~ 1 cm accuracy, which is very challenging. However, the complementary application of using VLBI to accurately track spacecraft holds great promise (Duev et al. 2012).

VSOP/HALCA was a space-VLBI mission launched in 1997. Using VSOP, Guirado et al. (2001) conducted space-VLBI astrometry of the radio QSO pair B1342+662/B1342+663 (which are only 5 arcmin apart) and demonstrated that the satellite position error was ~ 3 meters and that the useful astrometry could be accomplished only for very close pairs. Because of the poor performance of the VSOP 22 GHz receiving system, maser astrometry was not attempted.

Currently the Russian space-VLBI satellite, RadioAstron, is in orbit (with a maximum interferometric baseline of $\sim 300,000$ km, comparable to the Earth-Moon separation). Fringes from space-baselines have been obtained (Kardashev et al. 2013) and, perhaps, high-accuracy space-VLBI astrometry can be realized.

6.2 The Event Horizon Telescope

At millimeter and sub-mm wavelengths, VLBI can achieve an angular resolution sufficient to resolve event-horizon scales for nearby super-massive black holes. A prediction of general relativity is that at this scale one should see the "shadow" of the black hole (Falcke, Melia & Agol 2000). Impressive results have been achieved using *ad hoc* arrays of antennas that can observe at the short wavelengths required to "see through" a screen of electrons that blurs the image of Sgr A*, the super-massive black hole at the center of the Milky Way (Doeleman et al. 2008).

The Event Horizon Telescope is a world-wide collaboration to realize a powerful VLBI array operating at 1 mm or shorter wavelengths, anchored by the phased-ALMA (acting as a single telescope with great collecting area). In addition to imaging event horizon scales for Sgr A* and M 87, one should be able to explore the detailed structure of accretion disks and jet launching points in the vicinity of these super-massive black holes using multi-frequency astrometry. Broderick, Loeb & Reid (2011) investigated the possibility of such observations by using the sub-array mode of ALMA, SMA, CARMA and other telescopes and demonstrated that astrometry at the ~ 3 μas level is possible. With such accuracy one can trace positional variations of the black holes owing to perturbations from surrounding stars and/or a black hole companion. In addition, one should be able to monitor structural variations occurring on dynamical timescales of the innermost stable circular orbit, which for Sgr A* would be ~ 10 min.

6.3 Square Kilometer Array

The Square Kilometer Array (SKA) is a world-wide project to build and operate the next generation of radio interferometers with an aggregate collecting area ~ 1 km^2. Achieving the SKA will likely require three independent arrays, using different technologies to cover the frequency range of ~ 100 MHz to ~ 20 GHz. Micro-arcsecond astrometry can be achieved at frequencies above ~ 3 GHz, provided baselines of several thousand km are an integral part of the design. For astrometric observations, the SKA holds the promise of significantly increased relative positional accuracy, because its great sensitivity allows the use of weak calibrators much closer in angle on the sky to the astrometric target. Compared to the VLBA, for example, the increased sensitivity of the full SKA should allow the use of background compact radio sources at least an order of magnitude closer to the target, resulting in astrometric accuracy better than ± 1 μas! In addition, if multi-beam feeds are used on individual antennas, one could simultaneously observe many sources, greatly increasing astrometric survey speed.

Acknowledgment

MH would like to thank Nobuyuki Sakai, Naoko Matsumoto, Kazuhiro Hada, Hikaru Chida, Osamu Kameya, Fuyuhiko Kikuchi, and Yuka Oizumi for their support in preparing the manuscript. MH also acknowledges financial support by the MEXT/JSPS KAKENHI Grant Numbers 24540242 and 25120007.

Literature Cited

1. André, P, Men'schikov, A, Bontemps, S, et al.2010. *Astron. Astrophys.* 518:L102
2. Ando K, Nagayama T, Omodaka T, Handa T, Imai H, et al. 2011. *Publ. Astron. Soc. Jpn.* 63:45-51
3. Antreasian PG, Baird DT, Border JS, Burckhart PD, Graat EJ, et al. 2005. *SpRo* 42:394–405
4. Asada H. 2002, *Ap.J.* 574:L69–70
5. Asaki Y, Sudou H, Kono Y, Doi A, Dodson R, et al. 2007. *Publ. Astron. Soc. Jpn.* 59:397–418
6. Asaki Y, Deguchi S, Imai H, Hachisuka K, Miyoshi M, Honma M. 2010. *Ap.J.* 721:267–77
7. Bailes M, Manchester R, Kesteven M, Norris RP, Reynolds JE. 1990. *Nature* 343:240–1
8. Bailes M, Manchester R, kesteven MJ, Norris RP, Revnolds JE. 1990. *MNRAS* 247:322
9. Bartel N, Herring TA, Ratner MI, Shapiro II, Corey BE. 1986. *Nature* 319:733–83
10. Bartel N, Bietenholz MF, Lebach DE, Lederman JI, Petrov L, et al. 2012. *Ap. J. suppl.* 201:3
11. Bartkiewicz, A, Brunthaler, A, Szymczak, M, van Langevelde, HJ, Reid, MJ. 2008. *Astron. Astrophys.* 490:787–92
12. Beasley, AJ, Conway, JE. 1995. *Astron. Soc. Pac. Conf. Ser.* 82:328–343
13. Bietenholz MF, Bartel N, Rupen MP. 2004. *Ap.J.* 615:173–80
14. Bietenholz MF, Kondratiev V, Ransom S, Slane P, Bartel N, Buchner S. 2013. *MNRAS* 431:2590–8

15. Blandford, RD, Königl, A. 1979. *Ap. J.* 232:34-48
16. Border JS, Folkner WM, Kahn RD, Zukor KS. 1992. *TDAPR* 42:110
17. Bourda, G, Collioud, A, Charlot, P, Porcas, R, Garrington, S. 2011. *Astron. Astrophys.* 526:102
18. Bower GC, Bolatto A, Ford EB, Kalas P. 2009. *Astron. J.* 701:1922-39
19. Bower GC, Bolatto A, Ford EB, Fries A, Kalas P, et al. 2011. *Astron. J.* 740:32
20. Braatz, JA, Reid, MJ, Humphreys, EML, Henkel, C, Condon, JJ, Lo, KY. 2010. *Ap.J.* 718:657–65
21. Braatz, J, Reid, M, Kuo, CY, Impellizzeri, V, Condon, J, et al. 2013. *IAUS* 289:255
22. Brisken WF, Benson JM, Beasley AJ, Fromalont EB, Goss WM, Thorsett SE. 2000. *Ap.J.* 541:959–62
23. Brisken WF, Benson JM, Goss WM, Thorsett SE. 2002. *Ap.J.* 571:906–17
24. Brisken WF, Thorsett S, Golden A, Goss WM. 2003. *Ap.J.* 593:89–92
25. Brisken WF, Macquart JP, Gao JJ, Rickett BJ, Coles WA, et al. 2010. *Ap.J.* 708:232–43
26. Broderick AE, Loeb A, Reid MJ, 2011. *Ap.J.* 735:57
27. Brunthaler, A, Reid, MJ, Falcke, H, Greenhill, LJ, Henkel, C. 2005 *Science* 307:1440–3
28. Brunthaler, A, Reid, MJ, Falcke, H, Henkel, C, Menten, KM. 2005 *Astron. Astrophys.* 462:101–6
29. Brunthaler, A, Reid, MJ, Menten, KM, Zheng, XW, Moscadelli, L, Xu, Y. 2009. *Ap. J.* 693:424–9
30. Caballero-Nieves, SM, Gies, DR, Bolton, CT, et al. 2009. *Ap. J.* 701:1895–905
31. Campbell R, Bartel N, Shapiro II, Ratner MI, Cappallo RJ, et al. 1996. *Ap. J. Lett.* 461:95
32. Cernis, K. 1990. *Astrophys. Space Sci.* 166:315–30
33. Chatterjee S, Brisken WF, Vlemmings WHT, Goss WM, Lazio TJW. 2009. *Ap.J.* 698:250-65
34. Chatterjee S, Cordes JM, Vlemmings WHT, Arzoumanian Z, Goss WM, Lazio TJW. 2004. *Ap.J.* 604:339-45
35. Choi Y, Hirota T, Honma M, Kobayashi H, Bushimata T, et al. 2008. *Publ. Astron. Soc. Jpn.* 60:1007–12
36. Clark, T. A. et al. 1976, A. J., 81, 599–603
37. Counselman CCIII, Hinteregger HF, King RW, Shapiro II. 1973. *Science* 181:772-4
38. Counselman CCIII. 1976. *Annu. Rev. Astron. Astrophys.* 14:197-214
39. Counselman CCIII, Gourevitch SA, King RW, Loriot GB, Prinn RG. 1979. *Science* 205:85-86
40. Damour, T, Taylor, JH. 1991. *Ap. J.* 366:501–11
41. Darling, J. 2011. *Ap.J.* 732:2
42. Deller AT, Bailes M, Tingay SJ. 2009. *Science* 323:1327-9
43. Deller AT, Tingay SJ, Bailes M, Reynolds JE. 2009. *Ap.J.* 701:1243-57
44. Deller A, Verbiest J, Tingay SJ, Bailes M. 2008. *Ap.J.* 685:67-70
45. Deller AT, Camilo F, Reynolds JE, Halpern JP. 2012. *Ap.J. Lett.* 748:L1
46. Deller AT, Archibald AM, Brisken WF, Chatterjee S, Janssen GH, et al. 2012. *Ap.J.* 756:L25
47. Dodson R, Legge D, Revnolds JE, McCulloch PM. 2003. *Ap.J.* 596:1137-41
48. Doeleman, SS, Weintroub, J, Rogers, AEE, Plambeck, R, Freund, R, et al. 2008. *Nature* 455:78–80
49. Duev DA, Calves GM, Pogrebenko SV, Gurvits LI, Cimó G, Bocanegra BT. 2012. *Astron. & Astrophys.* 541:43
50. Duncan RC, Thompson C. 1992. *Ap.J.*, 392:L9-12
51. Dyson, FW, Eddington, AS, Davidson, C. 1919. *Ap. J.* 220:291–333
52. Dzib, S, Loinard, L, Mioduszewski, AJ, Boden, AF, Rodríguez, LF, Torres, RM. 2010. *Ap. J.* 718:610–9
53. Dzib SA, Rodriguez LF, Loinard L, Mioduszewski AJ, Ortiz-Leon GN, Araudo AT. 2013. *Ap.J.* 763:139
54. Eiroa, C, Djupvik, AA, Casali, MM. 2008. *in Handbook of Star Forming Regions Vol. II* (Astronomical Society of the Pacific, ed. Bo Reipurth), 5:693–734
55. Evans, NJ II, Dunham, MM, Jorgensen, JK et al.2008. *Ap. J. Suppl.* 181:321–50
56. Everitt C, DeBra D, Parkinson B, Turneaure J, Conklin J, et al. 2011. *Phy. Rev. Lett.* 106:1
57. Falcke, H, Melia, F, Agol, E. 2000. ApJ 528:L13–6
58. Folkner WM, Border JS, Nandi S, Zukor KS. 1993. *TDAPR* 42-113:22-36
59. Fomalont EB, Goss WM, Beasley AJ, Chatterjee S. 1999. *Astron. J.* 117:3025-30

60. Fomalont EB, Kopeikin S. 2003. *Ap.J.* 598:704
61. Fomalont EB, Kopeikin S, Lanyi G, Benson J. 2009. *Ap.J.*, 699:1395
62. Fomalont, E., Kopeikin, S. 2009. *in Cosmology and Extragalactic Astgrophysics* (Proceedings of the IAU Symposium 240, eds. Jin, Platais & Perryman), 248:383–6
63. Gawronski, MP, Gozdziewski, K, Katarzynski, K. 2013, arXiv:1309:4639
64. Genzel, R, Reid, MJ, Moran, JM, Downes, D. 1981. *Ap. J.* 244:884–902
65. Ghez, AM, Salim, S, Weinberg, NN, et al. 2008. *Ap. J.* 689:1044–62
66. Gillessen, S, Eisenhauer, F, Trippe, S, et al.2009. *Ap. J.* 692:1074–109
67. Goossens S, Matsumoto K, Liu Q, Kikuchi F, Sato K, et al. 2011. *JGeod* 85:205-28
68. Gou, L, McClintock, JE, Reid, MJ, et al. 2011. *Ap. J.* 742:85
69. Güdel, M, Arzner, K, Audard, M, et al.2008. *Astron. Soc. Pac. Conf. Ser.* 384:65–9
70. Guirado JC, Marcaide JM, Alberdi A, Elosegui P, Ratner MI, et al. 1995. *Astron. J.*110:2586
71. Guirado JC, Reynolds JE, Lestrade JF, Preston RA, Jauncey DL, et al. 1997. *Ap.J.*, 490:835–9
72. Guirado JC, Ros E, Jones DL, Lestrade JF, Marcaide JM, et al. 2001. *Astron. & Astrophys.* 371:766-70
73. Gwinn C, Taylor J, Weisberg JM, Rawley LA. 1986. *Astron. J.* 91:338–42
74. Hada K, Doi A, Kino M, Nagai H, Hagiwara Y, Kawaguchi N. 2011. *Nature*477:185–7
75. Hada K, Kino M, Nagai H, Doi A, Hagiwara Y, et al. 2012. *Ap.J.* 760:52
76. Harrison, TE, McNamara, BJ, Szkody, P., et al. 1999. *Ap. J.* 515:L93–6
77. Hachisuka, K, Brunthaler, A, Menten, KM, Reid, MJ, Imai, H, et al. 2006. *Ap. J.* 645:337–44
78. Hachisuka, K, Brunthaler, A, Menten, KM, Reid, MJ, Hagiwara, Y, Mochizuki, N. 2009. *Ap. J.* 696:1981–6
79. Helfand D, Chatterjee S, Brisken WF, Camilo F, Reynolds J, et al. 2007. *Ap.J.* 662:1198–203
80. Herbig, GH, Jones, BF. 1983. *A. J.* 88:1040–52
81. Hernández-Pajares M, Juan JM, Sanz J, Orus R, Garcia-Rigo A, et al. 2009. *J. Geod.* 83:265-75
82. Herrnstein, JR, Moran, JM, Greenhill, LJ, Diamond, PJ, et al. 1999. Nature 400:539–41
83. Herrnstein, JR, Moran, JM, Greenhill, LJ, Trotter, AS. 2005. Ap. J. 629:719–38
84. Hildebrand CE, Iijima BA, Kroger PM, Folkner WM, Edwards CD. 1994. *TDAPR* 119:46–82
85. Hirshfeld, A. "Parallax: The Race to Measure the Cosmos", 2001, W.H. Freeman & Co., NY
86. Hirota, T, Bushimata, T, Choi, YK, et al. 2007. *Pub. Astron. Soc. Japan* 59:897–903
87. Hirota, T, Bushimata, T, Choi, YK, et al. 2008. *Pub. Astron. Soc. Japan* 60:37–44
88. Hirota, T, Honma, M, Imai, H. 2011. *Pub. Astron. Soc. Japan* 63:1–8
89. Honma, M, Fujii, T, Hirota, T., et al. 2003. *Pub. Astron. Soc. Japan* 55:L57–60
90. Honma, M, Bushimata, T, Choi, YK, Hirota, T, Imai, H, et al. 2007. *Publ. Astron. Soc. Jpn.* 59:889–95
91. Honma M, Kijima M, Suda H, Kawaguchi N, Kobayashi H, et al. 2008a. *Publ. Astron. Soc. Jpn.* 60:935–50
92. Honma, M, Tamura, Y, Reid, MJ. 2008b. *Pub. Astron. Soc. Japan* 60:951–960
93. Honma M, Hirota T, Kan-Ya Y, Kawaguchi N, Kobayashi H, et al. 2011. *Publ. Astron. Soc. Jpn.* 63:17–22
94. Honma, M, Nagayama, T, Ando, K, Bushimata, T, Choi, YK, et al. 2012. *Pub. Astron. Soc. Japan* 64:136
95. Hubble, EP. 1926. *Ap. J.* 63:236–74
96. Humphreys, EML, Reid, MJ, Moran, JM, Greenhill, LJ, Argon, AL. 2013. *Ap. J.* 775:13
97. Imai, H, Nakashima, K, Bushimata, T, et al. 2007. *Pub. Astron. Soc. Japan* 59:1107–13
98. Imai H, Sahai R, Morris M. 2007. *Ap.J.* 669:424–34
99. Imai H, Tafoya D, Honma M, Hirota T, Miyaji T. 2011. *Publ. Astron. Soc. Jpn.* 63:81–7
100. Imai H, Sakai N, Nakanishi H, Sakanoue H, Honma M, Miyaji T. 2012. *Publ. Astron. Soc. Jpn.* 64:142
101. Imai H, Kurayama T, Honma M, Miyaji T. 2013. *Publ. Astron. Soc. Jpn.* 65:28
102. Immer, K, Reid, MJ, Menten, KM, Brunthaler, A, Dame, TM. 2013. *Astron. Astrophys.* 553:117
103. Jacobson RA, Antreasian PG, Bordi JJ, Criddle KE, Ionasescu R, et al. 2006. *Astron. J.* 132:2520–6

104. Jones DL, Fomalont EB, Dhawan V, Romney J, Folkner WM, et al. 2011. *Astron. J.* 141:29
105. Kamezaki T, Nakagawa A, Omodaka T, Kurayama T, Imai H, et al. 2012. *Publ. Astron. Soc. Jpn.* 64:7
106. Kamohara R, Bujarrabal V, Honma M, Nakagawa A, Matsumoto N, et al. 2010. *Astron. & Astrophys.* 510:A69
107. Kardashev, N, Khartov, VV, Abramov, VV, Avdeev, VY, Alakoz, AV, et al. 2013. *Ast. Rep.* 57:153–94
108. Kikuchi F, Liu Q, Hanada H, Kawano N, Matsumoto K, et al. 2009. *RaSc* 44:2008–14
109. Kim, MK, Hirota, T, Honma, M, et al.2008. *Pub. Astron. Soc. Japan* 60:991–9
110. King RW, Counselman CCIII, Shapiro II. 1976. *JGR* 81:6251–6
111. Kovalev YY, Lobanov AP, Pushkarev AB, Zensus JA. 2008. *Astron. & Astrophys.* 483:759–86
112. Kuo, CY, Braatz, JA, Reid, MJ, Lo, KY, Condon, JJ, et al. 2013. *Ap. J.* 767,155
113. Kurayama T, Sasao T, Kobayashi H. 2005. *Ap.J.* 627:L49–52
114. Kurayama T, Nakagawa A, Sawada-Satoh S, Sato K, Honma M, et al. 2011. *Publ. Astron. Soc. Jpn.* 63:513-25
115. Lambert SB, Le Poncin-Lafitte C. 2009. *Astron. & Astrophys.*, 499:331–5
116. Lambert SB, Le Poncin-Lafitte C. 2011. *Astron. & Astrophys.*, 529:70
117. Langevelde HJ van, Vlemmings WHT, Diamond PJ, Baudry A, Beasley AJ. 2000. *Astron. & Astrophys.* 357:945–50
118. Lanyi G, Border J, Benson J, Dhawan V, Fomalont E, et al. 2005. *IPNPR* 162:1–16
119. Lanyi G, Bagri DS, Border J. 2007. *Proceedings of the IEEE*, 95:2193–201
120. van Leeuwen, F. 2009. *Astron. Astrophys.* 497:209–42
121. Lestrade JF, Phillips RB, Hodges MW, Preston RA. 1993. *Ap.J.* 410:808–14
122. Lestrade JF, Jones DL, Preston RA, Phillips RB, Titus MA, et al. 1995. *Astron. & Astrophys.* 304:182–8
123. Lestrade JF, Phillips RB, Jones DL, Preston RA. 1996. *J.Geo.Res.* 101:14837–42
124. Lestrade JF, Preston RA, Jones DL, Phillips RB, Rogers AEE, et al. 1999. *Astron. & Astrophys.* 344:1014–26
125. Loeb, A; Reid, MJ, Brunthaler, A, Falcke, H. 2005. *Ap. J.* 633:894–8
126. Loinard, L, Mioduszewski, AJ, Rodríguez, LF, González, RA, Rodríguez, MI, Torres, RM. 2005. *Ap. J.* 619:L179–L182
127. Loinard, L, Torres, RM, Mioduszewski, AJ, et al.2007. *Ap. J.* 671:546–54
128. Loinard, L, Torres, RM, Mioduszewski, AJ, Rodríguez, LF. 2008. *Ap. J.* 675:L29–L32
129. Ma, C. et al. 1986. *A. J.* 92:1020–1029
130. van Maanen, A. 1923. *Ap. J.* 57:264–78
131. Macri, LM, Stanek, KZ, Bersier, D, Greenhill, LJ, Reid, MJ. 2006. *Ap. J.* 652:1113–49
132. Marcaide JM, Shapiro II. 1984. *Ap.J.* 276:56–9
133. Marcaide, J. M. et al. 1985, Astron. Astrophys., 142:71–84
134. Marcaide JM, Elosegui P, Shapiro II. 1994. *Astron. J.* 108:368–73
135. Marti-Vidal I, Marcaide JM, Alberdi A, Pérez-Torres MA, Ros E, Guirado JC. 2011. *Astron. & Astrophys.* 533:A111
136. Marti-Vidal I, Marcaide JM, Guirado JC, Pérez-Torres MA, Ros E. 2008. *Astron. & Astrophys.* 478, 267–75
137. Matsumoto N, Honma M, Isono Y, Ujihara H, Kimura K, et al. 2011. *Publ. Astron. Soc. Jpn.* 63:1345-56
138. Melis et al. in preparation
139. Menten, KM, Reid, MJ, Eckart, A, Genzel, R. 1997. *Ap. J.* 475:L111–4
140. Menten, KM, Reid, MJ, Forbrich, J, Brunthaler, A. 2007. *Astron. Astrophys.* 474:515–20
141. Miller-Jones, JCA, Jonker, PG, Dhawan, V, Brisken, W, Rupen, MP, et al. 2013. *Ap. J.* 706:L230–4
142. Miller-Jones, JCA, Sivakoff, GR, Knigge, C, Körding, EG, Templeton, M, Waagen, EO. 2013. *Science* 340:950–2
143. Min CH, et al. 2013. *Publ. Astron. Soc. Jpn.*, submitted

144. Mirabel, FI, Rodrigues, I. 2003. *Science* 300:1119–20
145. Moellenbrock, GA, Claussen, MJ, Goss, WM. 2009. *Ap. J.* 694:192–204
146. Mori K, Gotthelf EV, Zhang S, An H, Baganoff FK, et al. 2013. *Ap. J. Lett.* 770:L23
147. Moscadelli, L, Cesaroni, R, Rioja, MJ, Dodson, R, Reid, MJ. 2011. *Astron. Astrophys.* 526:66
148. Motogi K, Sorai K, Habe A, Honma M, Kobayashi H, et al. 2011. *Publ. Astron. Soc. Jpn.* 63:31–44
149. Nagayama T, Omodaka T, Nakagawa A, Handa T, Honma M, et al. 2011. *Publ. Astron. Soc. Jpn.* 63:23–30
150. Nagayama T, Omodaka T, Handa T, Honma M, Kobayashi H, et al. 2011. *Publ. Astron. Soc. Jpn.* 63:719–25
151. Nakagawa A, Tsushima M, Ando K, Bushimata T, Choi YK, et al. 2008. *Publ. Astron. Soc. Jpn.* 60:1013–21
152. Ng, CY, Romani RW, Brisken WF, Chatterjee S, Kramer M. 2007. *Ap.J.* 654:487–93
153. Niinuma K, Nagayama T, Hirota T, Honma M, Motogi K, et al. 2011. *Publ. Astron. Soc. Jpn.* 63:9–16
154. Nyu D, Nakagawa A, Matsui M, Imai H, Sofue Y, et al. 2011. *Publ. Astron. Soc. Jpn.* 63:63–70
155. Oh CS, Kobayashi H, Honma M, Hirota T, Sato K, et al. 2010. *Publ. Astron. Soc. Jpn.* 62:101-14
156. Orosz, JA, McClintock, JE, Aufdenberg, JP, Remillard, RA, Reid, MJ, Narayan, R, Gou, L. 2011 *Ap. J.* 742:84
157. Peterson WM, Mutel RL, Lestrade JF, Güdel M, Goss WM. 2011. *Astron. J.* 737:104
158. Porcas RW. 2009. *Astron. & Astrophys.* 505:L1–4
159. Ratner MI, Bartel N, Bietenholz MF, Lebach DE, Lestrade JF, et al. 2012. *Ap. J. suppl.* 201:5
160. Reid, MJ, Schneps, MH, Moran, JM, Gwinn, CR, Genzel, R, et al. 1988. *Ap. J.* 330:809–16
161. Reid, MJ, Menten, KM, Genzel, R, Ott, T, Sch?del, R, Eckart, A. 2003. *Ap. J.* 587:208–20
162. Reid, MJ, Brunthaler, A. 2004 *Ap. J.* 616:872–84
163. Reid, MJ. 2009. *Int. J. Mod. Phys. D* 18:889-910
164. Reid, MJ, Menten, KM, Brunthaler, A, Zheng, XW, Moscadelli, L, Xu, Y. 2009a. *Ap. J.* 693:397–405
165. Reid, MJ, Menten, KM, Zheng, XW, Brunthaler, A, Moscadelli, L, et al. 2009b. *Ap. J.* 700:137–48
166. Reid, MJ, Braatz, JA, Condon, JJ, Greenhill, LJ, Henkel, C, Lo, KY. 2009c. *Ap. J.* 695:287–91
167. Reid, MJ, McClintock, JE, Narayan, R, Gou, L, Remillard, RA, Orosz, JA. 2011 *Ap. J.* 742:83
168. Reid, MJ, Braatz, JA, Condon, JJ, Lo, KY, Kuo, CY, et al. 2013. *Ap. J.* 767:154
169. Reid, MJ, et al. submitted to Ap. J.
170. Riess, AG, Fliri, J, Valls-Gabaud, D. 2012 *Ap. J.* 745:156
171. Riess, AG, Macri, L, Casterno, S, Lampeitl, H, Ferguson, HC, et al. 2012. *Ap. J.* 752:76
172. Rioja MJ, Marcaide JM, Elosegui P, Shapiro II. 1997. *Astron. & Astrophys.*325:383-90
173. Ros E, Marcaide JM, Guirado JC, Pérez-Torres MA. 2001. *Astron. & Astrophys.*376:1090-105
174. Rioja, M, Dodson, R, Porcas, RW, Ferris, D, Reynolds, J, et al. 2009, Proceedings of the 8th International e-VLBI Workshop. 22-26 June 2009. Madrid, Spain
175. Rygl KLJ, Brunthaler A, Sanna A, Menten KM, Reid MJ, et al. 2012. *Astron. & Astrophys.* 539:79.1-12
176. Rygl, KLJ, Brunthaler, A, Reid, MJ, Menten, KM, van Langevelde, HJ, Xu, Y. 2010. *Astron. Astrophys.* 511:2
177. Sagdeyev RZ, Kerzhanovitch VV, Kogan LR, Kostenko VI, Linkin VM, et al. 1992. *Astron. & Astrophys.* 254:387
178. Salzberg IM. 1973. *IEEEP* 61:1233-36
179. Sandstrom, KM, Peek JEG, Bower, GC, Bolatto, AD, Plambeck, RL. 2007. *Ap. J.* 667:1161–9
180. Sanna, A, Reid, MJ, Moscadelli, L, Dame, TM, Menten, KM, et al. 2009. *Ap. J.* 706:464–70
181. Sanna, A, Reid, MJ, Dame, TM, Menten, KM, Brunthaler, A, et al. 2012. *Ap. J.* 745:82
182. Sakai N, Honma M, Nakanishi H, Sakanoue H, Kurayama T, et al. 2012. *Publ. Astron. Soc. Jpn.* 64:108
183. Sato M, Hirota T, Honma M, Kobayashi H, Sasao T, et al. 2008. *Publ. Astron. Soc. Jpn.* 60:975-89
184. Sato, M, Reid, MJ, Brunthaler, A, Menten, KM. 2010a. *Ap. J.* 720:1055–65

185. Sato M, Hirota T, Reid MJ, Honma M, Kobayashi H, et al. 2010b. *Publ. Astron. Soc. Jpn.* 62:287-99
186. Schödel, R, Ott, T, Genzel, R, et al. 2002. *Nature* 419:694–6
187. Shapiro II, Wittels JJ, Counselman CCIII, Robertson DS, Whitney AR, et al. 1979. *Ap.J.* 84:1459-69
188. Shapiro II, Bartel N, Bietenholz MF, Lebach DE, Lestrade JF, et al. 2012. *Ap. J. suppl.* 201:1
189. Shiozaki S, Imai H, Tafoya D, Omodaka T, Hirota T, et al. 2011. *Publ. Astron. Soc. Jpn.* 63:1219-28
190. Slade MA, Preston RA, Harris AW, Skjerve LJ, Spitzmesser DJ. 1977. *Moon* 17:133-47
191. Soderblom, DR, Nelan, E, Benedict, GF, et al. 2005. *A. J.* 129:1616-24
192. Sokolovsky KV, Kovalev YY, Pushkarev AB, Lobanov AP. 2011. *Astron. & Astrophys.* 532:A38
193. Steigenberger P, Tesmer V, Krügel M, Thaller D, Schmid R, et al. 2007. *J.Geod.* 81:503-14
194. Tafoya D, Imai H, Gomez Y, Torrelles JM, Patel NA, et al. 2011. *Publ. Astron. Soc. Jpn.* 63:71-80
195. Thompson, AR, Moran, JM, Swenson, GW Jr. 2001. *Interferometry and Synthesis in Radio Astronomy, $2^n d$ edition.* New York, USA: John Wiley & Sons, Inc.
196. Torres, RM, Loinard, L, Mioduszewski, AJ, Rodríguez, LF. 2007. *Ap. J.* 671:1813–9
197. Torres, RM, Loinard, L, Mioduszewski, AJ, Rodríguez, LF. 2009. *Ap. J.* 698:242–9
198. Torres, RM, Loinard, L, Mioduszewski, AJ, et al.2012. *Ap. J.* 747:18
199. Vlemmings WHT, Langevelde HJ van, Diamond PJ, Habing HJ, Schilizzi RT. 2003. *Astron. & Astrophys.* 407:213-24
200. Vlemmings WHT, Langevelde HJ Van. 2007. *Astron. & Astrophys.* 472:547-53
201. Wade, C, Johnston, KJ. 1977, A. J., 82, 791–795
202. Walker, RC, Chatterjee, S. 2000, VLBA Scientific Memo 23. http://www.nrao.edu/memos/sci/gps_ion.html
203. Whitelock PA, Feast MW, Van Leeuwen F. 2008. *MNRAS* 386:313-23
204. Will CM. 2003. *Ap. J.* 590:683–90
205. Witasse O, Lebreton JP, Bird MK, Dutta-Roy R, Folkner WM, et al. 2006. *JGR* 111:E07S01
206. Xu, Y, Reid, MJ, Menten, KM, Zheng, XW. 2006. *Science* 311:54–7
207. Xu, Y, Reid, MJ, Menten, KM, Brunthaler, A, Zheng, XW, Moscadelli, L. 2009. *Ap. J.* 693:413–8
208. Xu, Y, Moscadelli, L, Reid, MJ, Menten, KM, Zhang, B, et al. 2009. *Ap. J.* 733:25
209. Xu, Y, Li, JJ, Reid, MJ, Menten, KM, Zheng, XW, et al. 2013. *Ap. J.* 769:15
210. Zhang, B, Zheng, XW, Reid, MJ, Menten, KM, Xu, Y, et al. 2009. *Ap. J.* 693:419–23
211. Zhang B, Reid MJ, Menten KM, Zheng XW. 2012. *Ap.J.* 744:23
212. Zhang B, Reid MJ, Menten KM, Zheng XW, Brunthaler A. 2012. *Astron. & Astrophys.* 544:A42
213. Zhang B, Reid MJ, Menten KM, Zheng XW, Brunthaler A., et al. 2013. *Ap. J.* 775:79